NSWCDD/TR-93/29

INCORPORATION OF BOUNDARY LAYER HEATING PREDICTIVE METHODOLOGY INTO NSWCDD AEROPREDICTION CODE

BY ROY M. MCINVILLE   FRANK G. MOORE
WEAPONS SYSTEMS DEPARTMENT

FEBRUARY 1993

NSWC
Naval Surface Warfare Center
DAHLGREN DIVISION

NAVAL SURFACE WARFARE CENTER
DAHLGREN DIVISION
Dahlgren, Virginia 22448-5000

NSWCDD/TR-93/29

INCORPORATION OF BOUNDARY LAYER HEATING PREDICTIVE METHODOLOGY INTO NSWCDD AEROPREDICTION CODE

BY ROY M. MCINVILLE   FRANK G. MOORE
WEAPONS SYSTEMS DEPARTMENT

FEBRUARY 1993

NAVAL SURFACE WARFARE CENTER
DAHLGREN DIVISION
Dahlgren, Virginia 22448-5000

FOREWORD

This report describes a part of the ongoing effort to make the latest version of the Naval Surface Warfare Center, Dahlgren Division (NSWCDD) aeroprediction code more applicable to the high Mach number range often associated with modern weapon systems. The methods presented enable the computation of three-dimensional heat transfer rates and recovery temperatures as part of the overall high Mach number solution.

The work described in this report was supported primarily through the Office of Naval Research (Dave Siegel, Code 213) and, more specifically, the Surface-Launched Weapons Technology Block Program managed at NSWCDD by Robin Staton. Partial funding for comparisons of the new predictive techniques to other methods was provided by the Strategic Defense Project Office. These funds are managed at NSWCDD by George Long, G205, in support of program leadership by Pete Stafford, K105. Appreciation is expressed to these individuals.

This report has been reviewed by Thomas J. Rice, Head, Aeromechanics Branch and Danny L. Brunson, Head, Missile Systems Division.

Approved by:

David S. Malyevac

DAVID. S. MALYEVAC, Deputy Department Head
Weapons Systems Department

ABSTRACT

Methods have been incorporated into the Naval Surface Warfare Center, Dahlgren Division aeroprediction code to permit the computation of heat transfer rates and recovery temperatures as part of the high Mach number solution. A mass balance technique has been included to determine the correct boundary layer edge entropy to use along the surface of blunt bodies. Refinements were also made to the pressure prediction routines to remove discontinuities and improve overall results. Comparisons of results from the new methods with those from more advanced engineering codes, with other techniques of similar technical level of detail, and with experimental data show good agreement. These new capabilities make possible the rapid computation of three-dimensional heat transfer information for a wide range of geometric configurations and flight conditions.

CONTENTS

Section		Page
1.0	BACKGROUND	1-1
2.0	INTRODUCTION	2-1
3.0	HEAT TRANSFER COEFFICIENTS	3-1
4.0	BOUNDARY LAYER HEATING METHODS	4-1
	4.1 NOSE TIP STAGNATION POINT	4-1
	4.2 CONTROL SURFACE LEADING EDGE STAGNATION LINE	4-4
	4.3 BODY	4-10
	4.4 CONTROL SURFACES	4-14
5.0	RESULTS	5-1
	5.1 STAGNATION POINT	5-1
	5.2 STAGNATION LINE	5-3
	5.3 SHARP CONE	5-5
	5.4 SHARP WEDGES	5-6
	5.5 SPHERICALLY BLUNTED CONES	5-7
6.0	SUMMARY	6-1
7.0	REFERENCES	7-1
8.0	SYMBOLS	8-1
APPENDIXES		
	A–MODIFICATIONS TO PRESSURE METHODOLOGY	A-1
	B–ENTROPY LAYER EFFECTS	B-1
DISTRIBUTION		(1)

ILLUSTRATIONS

Figure		Page
5-1	HEAT TRANSFER RATES FOR 0.375-IN. NOSE RADIUS 15-DEG HALF-ANGLE CONE AT $\alpha = 20$ DEG	5-8
5-2	HEAT TRANSFER RATES FOR 1.1-IN. NOSE RADIUS 15-DEG HALF-ANGLE CONE AT $\alpha = 5$ DEG	5-10
5-3	HEAT TRANSFER RATES FOR 1.1-IN. NOSE RADIUS 15-DEG HALF-ANGLE CONE AT $\alpha = 10$ DEG	5-10
5-4	CIRCUMFERENTIAL VARIATION OF HEATING RATES ON 1.1-IN. NOSE RADIUS 15-DEG HALF-ANGLE CONE AT $\alpha = 5$ DEG, $x/r_N = 4.86$	5-11
5-5	CIRCUMFERENTIAL VARIATION OF HEATING RATES ON 1.1-IN. NOSE RADIUS 15-DEG HALF-ANGLE CONE AT $\alpha = 5$ DEG, $x/r_N = 10.13$	5-11
5-6	CIRCUMFERENTIAL VARIATION OF HEATING RATES ON 1.1-IN. NOSE RADIUS 15-DEG HALF-ANGLE CONE AT $\alpha = 10$ DEG, $x/r_N = 4.86$	5-12
5-7	CIRCUMFERENTIAL VARIATION OF HEATING RATES ON 1.1-IN. NOSE RADIUS 15-DEG HALF-ANGLE CONE AT $\alpha = 10$ DEG, $x/r_N = 10.13$	5-12

TABLES

Table		Page
5-1	NOSE STAGNATION POINT COMPARISONS, $M_\infty = 7.73$, ALTITUDE = 82,500 FT, NOSE RADIUS = 0.01 IN., AND SURFACE TEMPERATURE = 580 °R	5-2
5-2	NOSE STAGNATION POINT COMPARISONS, $M_\infty = 10$, ALTITUDE = 82,500 FT, NOSE RADIUS = 0.01 IN., AND SURFACE TEMPERATURE = 580 °R	5-2

TABLES (CONTINUED)

Table		Page
5-3	NOSE STAGNATION POINT COMPARISONS, $M_\infty = 15$, ALTITUDE = 82,500 FT, NOSE RADIUS = 0.01 IN., AND SURFACE TEMPERATURE = 580 °R	5-2
5-4	SWEPT CYLINDER STAGNATION LINE COMPARISONS, $M_\infty = 7.73$, ALTITUDE = 82,500 FT, CYLINDER RADIUS = 0.01 IN., SWEEP ANGLE = 53.13 DEG, AND SURFACE TEMPERATURE = 580 °R	5-3
5-5	SWEPT CYLINDER STAGNATION LINE COMPARISONS, $M_\infty = 10$, ALTITUDE = 82,500 FT, CYLINDER RADIUS = 0.01 IN., SWEEP ANGLE = 53.13 DEG, AND SURFACE TEMPERATURE = 580 °R	5-3
5-6	SWEPT CYLINDER STAGNATION LINE COMPARISONS, $M_\infty = 15$, ALTITUDE = 82,500 FT, CYLINDER RADIUS = 0.01 IN., SWEEP ANGLE = 53.13 DEG, AND SURFACE TEMPERATURE = 580 °R	5-4
5-7	SWEPT CYLINDER STAGNATION LINE COMPARISONS, RADIUS = 0.5 IN., ALTITUDE = 82,500 FT, SWEEP ANGLE = 53.13 DEG, AND SURFACE TEMPERATURE = 580 °R	5-4
5-8	SWEPT CYLINDER STAGNATION LINE COMPARISONS, RADIUS = 1.0 IN., ALTITUDE = 82,500 FT, SWEEP ANGLE = 53.13 DEG, AND SURFACE TEMPERATURE = 580 °R	5-4
5-9	30-DEG SHARP-CONE COMPARISONS, $M_\infty = 7.73$, ALTITUDE = 82,500 FT, SURFACE TEMPERATURE = 836 °R, AND S = 1.75 IN.	5-5
5-10	30-DEG SHARP-CONE COMPARISONS, $M_\infty = 10$, ALTITUDE = 82,500 FT, SURFACE TEMPERATURE = 1200 °R, AND S = 1.75 IN.	5-5
5-11	30-DEG SHARP-CONE COMPARISONS, $M_\infty = 15$, ALTITUDE = 82,500 FT, SURFACE TEMPERATURE = 3658 °R, AND S = 1.75 IN.	5-6
5-12	4-DEG SHARP-WEDGE COMPARISONS, $M_\infty = 7.73$, ALTITUDE = 82,500 FT, SURFACE TEMPERATURE = 580 °R, AND S = 0.655 IN.	5-6

TABLES (CONTINUED)

Table		Page
5-13	4-DEG SHARP-WEDGE COMPARISONS, $M_\infty = 10$, ALTITUDE = 82,500 FT, SURFACE TEMPERATURE = 580 °R, AND S = 0.655 IN.	5-7
5-14	4-DEG SHARP-WEDGE COMPARISONS, $M_\infty = 15$, ALTITUDE = 82,500 FT, SURFACE TEMPERATURE = 580 °R, AND S = 0.655 IN.	5-7

1.0 BACKGROUND

The accelerating pace of technological advances in recent years has given rise to a new generation of potential military threats for which appropriate countermeasures must be developed. In the case of surface-launched tactical missiles, the new targets that must be intercepted are faster, more maneuverable, and more difficult to detect and track. Many design and operational factors must be considered if successful engagements are to be possible under these conditions. One of the more critical concerns lies in the severe aerodynamic environment to which the missile is exposed as a result of the high velocities needed to deal with sophisticated targets that may be approaching quite rapidly and may only be detected at relatively close range. Depending on the given situation, effective defensive measures could call for a missile capable of upper supersonic or even hypersonic flight. This regime is currently being investigated by the U.S. Navy with designs under consideration, such as the antitactical ballistic missile (ATBM) and lightweight exo-atmospheric projectile (LEAP), which call for upper flight Mach numbers of around 15.

As the performance envelope is extended into the hypersonic region above Mach 6, two important aerodynamic phenomena become increasingly important. The first of these relates to the manner in which the air molecules in the vicinity of the missile store energy at the elevated temperatures created by the strong bow shock. At temperatures up to about 1400 °R, the heat dissipated by the shock is stored in the translational and rotational energy modes of the gas molecules. The fluid behavior is adequately described by the perfect gas law, and the specific heats remain constant. As the temperature rises, the vibrational energy modes of the molecules become excited. The perfect gas law is no longer valid, and the specific heats become functions of temperature. Above about 4500 °R, the air molecules begin to dissociate and chemical reactions occur leading to even greater complexities. This departure from perfect gas behavior is often referred to generically as *real-gas effects*. It tends to become significant above approximately Mach 6. The overall result is to lower the gas temperatures below those that would be predicted by a perfect gas analysis. The increase in modes of internal energy storage mean that less energy goes into the translational mode, which is directly measured as temperature. This effect will not be discussed in detail in this report other than in the context of the use of appropriate real-gas relations in high-temperature computations. For further information, Reference 1 provides a general discussion and Reference 2 explains in detail how the aeroprediction code has been modified to model real-gas physics.

The phenomenon described is characteristic of all high Mach number flows and is unrelated to the fluid viscosity. Thus, real-gas effects must be included even in inviscid flow models such as the Euler equations. The second effect that becomes important in high Mach number flows is related directly to the viscosity of the fluid. Boundary layer theory tells us that the fluid particles in contact with the body surface are at rest relative to it. This is the viscous *no-slip* condition. However, in the case of supersonic or hypersonic flight, the particles at some distance above the surface are moving at high velocities. Thus, there is a region separating the body surface and the external flow within which the fluid particles are decelerated from some large velocity to rest. This is the classical boundary layer, and it is usually quite thin, although in some hypersonic flows, it can become more pronounced. The boundary layer is dominated by viscous shear forces that dissipate the kinetic energy of fluid particles approaching the surface. Energy cannot be destroyed, so this process results in an increase in the internal energy of the fluid, the magnitude of which is directly related to the kinetic energy of the external flow. This increase in internal energy appears in the form of a rise in boundary layer temperature and, because kinetic energy is proportional to the square of the velocity, it is apparent that as the Mach number increases, the boundary layer temperature can increase rapidly, leading to greater transfer of heat to the body surface. The Mach number at which this boundary layer heating becomes an important factor is dependent on a number of factors, such as the composition and structure of the missile, time of flight, internal environmental constraints, etc. In some situations, it can become significant at supersonic velocities. At hypersonic Mach numbers, it cannot be ignored under any circumstances.

This report describes the methodology that has been incorporated into the aeroprediction code to provide estimates of the boundary layer heating. Comparisons are presented with results from an approximate, point-solution aeroheating code (MINIVER) and several more sophisticated viscous flow solvers, as well as with experimental results. A comparison with inviscid flow properties computed by MINIVER is also presented to validate the real-gas techniques previously incorporated into the aeroprediction code.

2.0 INTRODUCTION

The task of generating numerical predictions of boundary layer heating can be approached in several ways. The most rigorous treatment involves a solution of the complete time-dependent Navier-Stokes equations including chemically reacting species if the temperatures are sufficiently high. Given present computer resources, this approach is much too costly to be used as a general engineering tool, requiring several hours of computational time and several megawords of memory on a super-computer. It would have to be reserved for a select number of special cases with complicating factors, such as flow separations or shock-boundary layer interactions, which are not amenable to simpler solution tactics.

If the full equations are simplified by dropping the streamwise (and, in some formulations, the crossflow) viscous terms, the resulting Thin Layer Navier-Stokes equations are somewhat easier to handle while still giving excellent results for most external flows. However, the solutions are costly, requiring only slightly less computer time and storage than the complete equations and so are still not suitable for routine engineering use.

Further simplification can be achieved by dropping the time-dependent terms to produce the Parabolized Navier-Stokes (PNS) equations. Obviously, these are valid only for steady flows, but they achieve great savings in computer resources by allowing space-marched solutions that require storage of only two or three crossflow planes of the computational grid at once instead of the entire field. This method cannot be applied if there are streamwise separations or regions where the flow exterior to the boundary layer is subsonic. The PNS equations can be a useful tool during the design process, but with computation times measured in minutes or even hours, the cost still precludes their use in the preliminary phase to generate large matrices of data for multiple configurations.

With a final simplification of dropping the viscous terms entirely, the widely used Euler equations are obtained. If the time-dependent terms are retained, it is possible to model unsteady and subsonic flows. Without these terms, only steady supersonic flows can be handled, but it becomes possible to use a rapid space-marched solution technique. If the interest is only in the surface pressures on the given missile, these equations can provide good solutions, but if viscous heating effects are important, the inviscid Euler results must be coupled to a boundary layer solver of some type. This approach is possible because of the relative weakness of the viscous-inviscid interactions in many problems. To a first approximation, there is no pressure change across the boundary layer allowing the use of the Euler surface pressures for all boundary layer computations. In addition, at sufficiently high Reynolds numbers, the boundary layer thickness is small in relation to the dimensions of the missile body. Thus, the viscous surface layer has no significant effect on the shape of the body as seen by the outer inviscid flow. The Euler equations can be solved to get the outer flow field and the computed surface pressures and velocities can be used as upper edge conditions for the boundary layer solution. Even if the boundary layer thickness increases to the point that it may no longer be considered *thin*, it may still be possible to use this coupled approach by employing an iterative sequence in which

1. Inviscid flow is computed with the Euler equations.

2. Boundary layer equations are solved using the inviscid surface conditions as inputs giving, among other things, the boundary layer thickness.

3. Adjustments are made to the body shape reflecting the displacement effect of the boundary layer.

4. The sequence is repeated until convergence is achieved.

At higher hypersonic Mach numbers, the boundary layer can occupy a significant portion of the space between the body and the shock or, in some cases, the outer edge of the boundary layer may merge with the shock. When the viscous-inviscid interaction becomes this strong, even the iterative approach no longer gives good results, and one of the previously discussed methods would have to be used.

The Euler equations are used on a fairly routine basis at all stages of the design and engineering process to generate force and moment data for aerodynamic bodies. The coupled Euler/boundary layer approach can provide good estimates of surface heating over a wide range of conditions, but depending on the particular combination of solvers used, it can require computer resources on the order of those used for the PNS equations. Using space-marched Euler and integral boundary layer methods, computational costs can be reduced to the point that engineering applications become possible, but a typical run to get the surface heating over a generic missile shape for a single Mach number-altitude combination can still require computational times of several minutes. Thus, this approach may also prove to be unsuitable for use in preliminary design investigation.

Before the advent of modern high-speed supercomputers, many approximate analytical techniques were developed to model the characteristics of a wide range of specialized aerodynamic flows. By making certain simplifying assumptions, the complexity of the governing equations was reduced to a level that could be handled easily by the available tools—often nothing more than hand computations being required. This report will not attempt to present a survey of such techniques but will make reference only to those that bear directly on the aeroprediction viscous heating modifications. It is important to point out that such techniques exist and that they produce acceptable results as long as their range of application does not go beyond the restricting conditions inherent in their development. A number of computer codes have been put together using such techniques, combining several analytical methods and, perhaps, some empirical databases to cover a range of aerodynamic conditions and geometric configurations. The major advantage of this approach lies in its speed, permitting computations in seconds or even fractions of a second on any mainframe computer or workstation. Their obvious drawback lies in their limited range of validity, but these limitations often are not severe, and a large percentage of problems likely to be encountered lend themselves to such treatment.

The aeroprediction code[3,4,5] is a collection of approximate techniques put together by Naval Surface Warfare Center, Dahlgren Division (NSWCDD) personnel to generate force and moment data for a wide variety of geometric configurations over a velocity range from subsonic to Mach 20. Limited capabilities are also available for computing skin friction drag, but no viscous heating methods have previously been incorporated. Over the years, it has proven to be an effective design tool and has been distributed to approximately 50 private, governmental, and international clients.[6] It has been the subject of several upgrades to extend its range of application, the most recent of these being the incorporation of high-temperature, real-gas effects into its second-order shock methodology, thus extending its usefulness into the hypersonic velocity regime.[2] As pointed out previously, at these high Mach numbers, boundary layer heating becomes a dominant factor in airframe design considerations. Because this was not an area that had been addressed in previous aeroprediction code evolution, it was decided that addition of this capability would make the high Mach number version a much more useful tool. In keeping with other aeroprediction methodologies, the viscous heating computations were to be implemented using approximate analytical techniques requiring a minimum of computer resources to execute. The following sections describe in detail how this goal was achieved.

3.0 HEAT TRANSFER COEFFICIENTS

The boundary layer heating information is presented in the aeroprediction output in the form of a heat transfer coefficient and an adiabatic wall temperature (also known as the recovery temperature) at each computational point. These variables are related in the following manner.

$$H = \frac{\dot{q}_w}{(T_{aw} - T_w)} \tag{3-1}$$

where H is the heat transfer coefficient, q_w is the surface heat transfer rate, T_{aw} is the adiabatic wall temperature, and T_w is the wall temperature. The adiabatic wall temperature is defined as

$$T_{aw} = T_e + r_c(T_0 - T_e) \tag{3-2}$$

where T_e is the boundary layer edge temperature (inviscid solution surface temperature) and T_0 is the stagnation temperature. The recovery factor, r_c, is defined as

$$r_c = \frac{T_{aw} - T_e}{T_0 - T_e} \tag{3-3}$$

and is a measure of the degree of efficiency involved in converting the kinetic energy of the external flow into heat within the boundary layer. If this conversion were 100-percent efficient, the adiabatic wall temperature and the stagnation temperature would be the same. T_{aw} is the highest possible temperature that can be reached within the boundary layer and, by extension, this is the highest temperature to which the wall can be heated. The length of time required for the wall temperature to reach this upper limit is dictated by the rate of heat transfer, $\dot{q}_w$. If the surface actually reaches T_{aw}, it can be seen from Equation 3-1 that the heat transfer rate would go to zero, thus the term adiabatic wall temperature.

The heat transfer coefficient for high temperature flows is often expressed in terms of enthalpies as

$$\eta = \frac{\dot{q}_w}{h_{aw} - h_e} \tag{3-4}$$

where η is the enthalpy-based heat transfer coefficient, h_{aw} is the adiabatic wall enthalpy, and h_w is the enthalpy of the fluid at the body surface. In this case, h_{aw} is defined as

$$h_{aw} = h_e + r_c(h_0 - h_e) \tag{3-5}$$

and the recovery factor, r_c, is

$$r_c = \frac{h_{aw} - h_e}{h_0 - h_e} \tag{3-6}$$

At temperatures above about 1500 °R, the enthalpy formulation is the more rigorously correct of the two. Below that point, they are equivalent, because the specific heats of the gas are constant and $h = c_pT$. Within the code, all real-gas, high-temperature computations are performed using the enthalpy as the basic variable, but to maintain consistency with other codes in use at NSWCDD, the results are converted to the temperature form for output. In either case, the recovery factor can be related to the Prandtl number of the fluid by

$$r_c = \sqrt{Pr} \quad \text{(laminar)} \tag{3-7}$$

and

$$r_c = (Pr)^{1/3} \quad \text{(turbulent)} \tag{3-8}$$

The heat transfer is normalized in the form given by Equation 3-1 because the coefficient H remains fairly constant over a wide range of wall temperatures. The heat transfer itself varies from some maximum value at $T_w = 0$ (cold wall) to zero at $T_w = T_{aw}$ (adiabatic wall). Given H and T_{aw} for a designated Mach number, angle of attack, and altitude combination, it is possible to compute the actual heat transfer rate for any wall temperature. Then, given the composition and structure of the wall, its rate of temperature change can be determined. By performing these computations sequentially at a selected number of points along a missile's trajectory, a time history of the surface temperature over the body can be constructed.

4.0 BOUNDARY LAYER HEATING METHODS

The user has the option, specified in the input file, of using either perfect-gas or real-gas relations for any aeroprediction run. For a detailed discussion of the theoretical background of the two approaches and of the real-gas extensions applied to the second-order, shock-expansion theory in aeroprediction, refer to Reference 2. The important point to bear in mind is that as flight Mach numbers rise beyond about 6, real-gas effects become increasingly important. Pressures are affected to a minimal degree, but temperatures are lowered substantially at the higher Mach numbers as new modes of energy storage are excited in the gas. In the discussion that follows, both perfect-gas and real-gas methods will be set forth. Both are available for use in the code. The perfect-gas option gives faster run times when it can be applied, but it is not recommended above Mach 6.

4.1 NOSE TIP STAGNATION POINT

The free-stream flow is first passed through a normal shock using the appropriate aeroprediction subroutines. This process uses either real- or perfect-gas methods, depending on the choice of input options. The flow behind the shock is then fully described by the subroutine outputs that are (where the subscript two denotes conditions behind the shock)

v_2 = Velocity
ρ_2 = Density
h_2 = Enthalpy
e_2 = Internal energy
S_2 = Entropy
a_2 = Sonic velocity
γ_2 = Specific heat ratio
z_2 = Compressibility factor

Stagnation conditions behind the shock are needed, and these can be obtained by an isentropic compression of the flow to zero velocity. The stagnation pressure is given by

$$p_0 = p_2 + \frac{1}{2} \rho v_2^2 \tag{4-1}$$

This relation can be used because the flow behind the shock is subsonic. In fact, the higher the free-stream Mach number, the more subsonic the downstream flow. Thus, even though the Bernoulli relation is strictly valid only for incompressible flow, the low Mach numbers behind the shock minimize any compressibility effects as the gas is decelerated.[7] Thus, because the stagnation pressure can be computed and the stagnation entropy is known because the compression is isentropic, the remaining gas properties can be determined.

4.1.1 Perfect-Gas Stagnation Point Conditions

The specific heat ratio is assumed to be constant and equal to 1.4. Then

$$T_0 = T_2\left(1 + \frac{\gamma_2 - 1}{2} M_2^2\right) \tag{4-2}$$

$$\rho_0 = \frac{p_0}{RT_0} \tag{4-3}$$

$$c_p = \frac{\gamma_2}{\gamma_2 - 1} R \tag{4-4}$$

$$h_0 = c_p T_0 \tag{4-5}$$

$$v_0 = 0 \tag{4-6}$$

$$M_0 = 0 \tag{4-7}$$

$$z_0 = 1 \tag{4-8}$$

R is the gas constant.

4.1.2 Real-Gas Stagnation Point Conditions

For real-gas conditions, first compute the stagnation enthalpy.

$$h_0 = h_2 + \frac{v_2^2}{2} \tag{4-9}$$

Then, given p_0, a series of curve fits is used to obtain the remaining properties.[8,9]

$$\rho_0 = \rho_0(p_0, h_0) \tag{4-10}$$

$$T_0 = T_0(p_0, \rho_0) \tag{4-11}$$

$$e_0 = e_0(\rho_0, p_0) \tag{4-12}$$

$$S_0 = S_0(e_0, \rho_0) \tag{4-13}$$

$$a_0 = a_0(e_0, S_0) \tag{4-14}$$

$$z_0 = \frac{p_0}{\rho_0 R T_0} \tag{4-15}$$

$$\gamma_0 = \frac{a_0^2}{R T_0} \tag{4-16}$$

$$v_0 = 0 \tag{4-17}$$

$$M_0 = 0 \tag{4-18}$$

4.1.3 Stagnation Point Heating

Given either the perfect- or real-gas properties established in the preceding sections, the nose-tip stagnation point heating rate can be found from[1]

$$\dot{q}_w = 0.763\,Pr^{\,0.6}\sqrt{\rho_0\mu_0}\,\sqrt{\frac{du_e}{dx}}\,(h_{aw} - h_w) \tag{4-19}$$

Pr is the Prandtl number and is considered to be a constant 0.7 for the perfect-gas case and is found from the curve fits for a real gas.

$$Pr = Pr\,(T_0, \rho_0) \tag{4-20}$$

The coefficient of viscosity, μ_0, is determined from Sutherland's Law for perfect-gas runs but is computed from the curve fit relations for real gases.

$$\mu_0 = \mu_0\,(T_0, \rho_0) \tag{4-21}$$

The stagnation point streamwise velocity gradient, du_e/dx, can be expressed as

$$\frac{du_e}{dx} = \frac{1}{r_N}\sqrt{\frac{2\,(p_0 - p_\infty)}{\rho_0}} \tag{4-22}$$

where a spherical nose tip of radius r_N is assumed. If the aeroprediction input file specifies a sharp nose, r_N is set to 0.01 in. The adiabatic wall enthalpy, h_{aw}, is defined in Equation 3-5, and h_w is the enthalpy of the fluid at the wall temperature. There is only one form of Equation 4-19 for both laminar and turbulent flow. At the stagnation point, the flow will always be laminar.

4.2 CONTROL SURFACE LEADING EDGE STAGNATION LINE

It is assumed that control surfaces are located in a "+" configuration, and the boundary layer heating is computed at the midspan of the upper and lower horizontal panels. This arrangement is consistent with that presently employed in the high Mach number control surface subroutines in aeroprediction. These subroutines use a local method that starts from free-stream conditions, and then, using oblique shocks or Prandtl-Meyer expansions, turns the flow through the necessary angle to make it parallel to the surface. No interference effects are included. It is realized that this approach can be improved, and future work will be devoted to this area as circumstances permit.

The first step in the computations involves decomposing the free stream into components normal and parallel to the leading edge.

$$v_n = v_\infty \cos\Lambda \tag{4-23}$$

$$v_p = \sqrt{v_\infty^2 - v_n^2} \tag{4-24}$$

The n and p subscripts denote directions normal and parallel to the leading edge, respectively. Λ is the sweep angle with $\Lambda=0$ corresponding to no sweep. The normal velocity component is passed through a normal shock, which produces a set of downstream conditions as given.

$v_{DS,n}$ = Downstream component normal to leading edge
T_{DS} = Downstream temperature
p_{DS} = Downstream pressure
ρ_{DS} = Downstream density
h_{DS} = Downstream enthalpy
e_{DS} = Downstream internal energy
S_{DS} = Downstream entropy
a_{DS} = Downstream sonic velocity
γ_{DS} = Downstream specific heat ratio
z_{DS} = Downstream compressibility factor

v_P is not affected by the shock. Assuming that the leading edge is analagous to an infinite span cylinder, the shock wave will be parallel to the stagnation line. Because v_P is parallel to the shock, it will also be parallel to the stagnation line and, similarly, $v_{DS,n}$ will be normal to the stagnation line and must go to zero at the surface. This loss of velocity will be felt as an increase in the pressure. Thus, at the surface the result is

$$v_{DS}' = v_p \tag{4-25}$$

$$v_{DS,n} \rightarrow 0 \tag{4-26}$$

$$p_{DS}' = p_{DS} + \frac{1}{2}\rho_{DS} v_{DS,n}^2 \tag{4-27}$$

Equation 4-27 is a valid approximation because of the relatively low velocities involved, as argued previously. The prime superscript denotes conditions at the surface where the normal velocity has been reduced to zero. The other fluid properties can now be found.

4.2.1 Perfect-gas Stagnation Line Conditions

Again, assume a constant specific heat ratio of 1.4, then proceed as follows:

$$c_p = \frac{\gamma_{DS}}{\gamma_{DS}-1} R \tag{4-28}$$

$$M_n = \frac{v_{DS,n}}{a_{DS}} \tag{4-29}$$

$$T_{DS}' = T_{DS}\left(1 + \frac{\gamma_{DS} - 1}{2} M_n^2\right) \tag{4-30}$$

$$\rho_{DS}' = \frac{p_{DS}'}{RT_{DS}'} \tag{4-31}$$

$$h_{DS}' = c_p T_{DS}' \tag{4-32}$$

$$z_{DS}' = 1 \tag{4-33}$$

$$a_{DS}' = \sqrt{\gamma_{DS} R T_{DS}'} \tag{4-34}$$

$$M_{DS}' = \frac{v_{DS}'}{a_{DS}'} \tag{4-35}$$

$$e_{DS}' = h_{DS}' - \frac{p_{DS}'}{\rho_{DS}'} \tag{4-36}$$

$$S_{DS}' = S_{DS} \tag{4-37}$$

In addition to these variables, the swept leading edge heating computations require as input the stagnation conditions behind a normal shock at the free-stream Mach number. These are obtained in the same manner as described in Section 4.1.1. It is also necessary to determine the stagnation conditions behind the swept leading edge shock. For a perfect gas, they can be determined as follows:

$$p_0' = p_{DS}' \left(1 + \frac{\gamma_{DS}' - 1}{2} M_{DS}'^2\right)^{\frac{\gamma_{DS}'}{\gamma_{DS}' - 1}} \tag{4-38}$$

$$T_0' = T_{DS}' \left(1 + \frac{\gamma_{DS}' - 1}{2} M_{DS}'^2\right) \tag{4-39}$$

$$\rho_0' = \frac{p_0'}{R\, T_0'} \tag{4-40}$$

$$h_0' = c_p T_0' \tag{4-41}$$

$$v_0' = 0 \tag{4-42}$$

$$M_0' = 0 \tag{4-43}$$

$$z_0' = 1 \tag{4-44}$$

4.2.2 Real-Gas Stagnation Line Conditions

The real-gas computations begin with the determination of the enthalpy.

$$h_{DS}' = h_{DS} + \frac{1}{2} v_{DS,n}^2 \tag{4-45}$$

The entropy is known since the compression to the prime conditions is isentropic. Using the curve fit relations once again gives

$$\rho_{DS}' = \rho_{DS}' (p_{DS}', h_{DS}') \tag{4-46}$$

$$T_{DS}' = T_{DS}' (p_{DS}', \rho_{DS}') \tag{4-47}$$

$$a_{DS}' = a_{DS}'(p_{DS}', S_{DS}') \tag{4-48}$$

$$M_{DS}' = \frac{v_{DS}'}{a_{DS}'} \tag{4-49}$$

$$e_{DS}' = e_{DS}'(\rho_{DS}', p_{DS}') \tag{4-50}$$

$$\gamma_{DS}' = \frac{a_{DS}'^2}{R\,T_{DS}'} \tag{4-51}$$

$$z_{DS}' = 1 \tag{4-52}$$

The required stagnation conditions behind the free-stream normal shock are determined as in Section 4.1.2. It is not as straightforward to get the stagnation conditions behind the leading edge oblique shock. The Bernoulli relation cannot be used because the Mach number is too high to ignore compressibility effects. The supersonic relations for stagnation conditions cannot be used because they do not include real-gas effects. An isentropic compression to the known stagnation enthalpy using real-gas relations is required. Unfortunately, the available curve fits do not contain a function with this combination of variables. It was necessary to employ an iterative approach. First, a stagnation pressure was assumed. The value predicted by the supersonic flow formula was used as this initial guess. Then, using the available curve fits, a corresponding value of stagnation entropy was computed as follows:

$$\rho_0' = \rho_0'(p_0', h_0') \tag{4-53}$$

$$e_0' = e_0'(\rho_0', p_0') \tag{4-54}$$

$$S_0' = S_0'(e_0', \rho_0') \tag{4-55}$$

The entropy value was checked for agreement with the isentropic assumption. If it was not correct, a second stagnation pressure value was chosen and the process repeated. If the resulting entropy was still off, a variable secant iteration scheme was used to get the correct stagnation pressure. The remaining flow properties could then be determined using the curve fit relations.

$$T_0' = T_0'(p_0', \rho_0') \quad (4\text{-}56)$$

$$a_0' = a_0'(p_0', S_0') \quad (4\text{-}57)$$

$$\gamma_0' = \frac{a_0'^{\,2}}{RT_0'} \quad (4\text{-}58)$$

$$z_0' = \frac{p_0'}{\rho_0' T_0'} \quad (4\text{-}59)$$

$$v_0' = 0 \quad (4\text{-}60)$$

$$M_0' = 0 \quad (4\text{-}61)$$

4.2.3 Beckwith and Gallagher Swept Cylinder Heating

The method of Beckwith and Gallagher[10,11] is used to compute the leading edge heat transfer rate. For laminar flow, the stagnation line heating rate is given by

$$\dot{q}_{w,l} = 0.57\,Pr^{-0.6}\sqrt{\rho_0\mu_0}\,\sqrt{\frac{du_e}{dx}}\,(h_{aw} - h_w)\,(\cos\Lambda)^{1.1} \quad (4\text{-}62)$$

Equation 4-62 is identical to Equation 4-19 with the exception of the leading coefficient and the addition of the last term involving the cosine of the sweep angle. For turbulent flow, the relation is more complicated.

$$\dot{q}_{w,t} = 1.04\,Pr^{-0.6}\,\frac{(\rho^*\mu^*)^{0.8}}{(\mu_0')^{0.6}}\,(v_{DS}'\sin\Lambda)^{0.6}\left(\frac{du_e}{dx}\right)_{SL}^{0.2}(h_{aw} - h_w) \quad (4\text{-}63)$$

The * superscript denotes evaluation at the Eckert reference enthalpy[12] which is given by

$$h^* = 0.5\,(h_w + h_e) + 0.22\,(h_{aw} - h_e) \quad (4\text{-}64)$$

where h_e is the enthalpy at the outer edge of the boundary layer. For the perfect-gas case, it is acceptable to compute a reference temperature instead.

$$T^* = 0.5\,(T_w + T_e) + 0.22\,(T_{aw} - T_e) \tag{4-65}$$

The reference enthalpy is then found by multiplying T^* by the specific heat, c_p. The streamwise velocity gradient at the stagnation line is given by

$$\left(\frac{du_e}{dx}\right)_{SL} = \frac{1}{r_{LE}} \sqrt{\frac{2\,(p'_{DS} - p_\infty)}{\rho'_{DS}}} \tag{4-66}$$

where r_{LE} is the leading edge radius of the control surface (which is assumed to be cylindrical). If a sharp leading edge is specified in the input file, r_{LE} is set equal to 0.01 in. for the heating computations.

The laminar or turbulent status of the flow is determined by computing the Reynolds number based on the leading edge diameter and the free-stream conditions.

$$Re_D = \frac{\rho_\infty v_\infty D}{\mu_\infty} \tag{4-67}$$

If Re_D is below some user-specified lower limit, Re_L, the laminar heat transfer is used. If Re_D is greater than a specified upper limit, Re_U, the turbulent value is used. For transitional values of Re_D between Re_L and Re_U, the heat transfer is given by

$$\dot{q}_w = \dot{q}_{w,l} + \left(\frac{Re_D - Re_L}{Re_U - Re_L}\right)\dot{q}_{w,t} \tag{4-68}$$

4.3 BODY

For points on the body, conditions at the outer edge of the boundary layer must be known. In the case of pressure, the inviscid surface value can be used because, to first order, the pressure gradient across the boundary layer is zero. These pressures are known from the appropriate aeroprediction methods. During the course of the present work, some refinements were made to the blunt body pressure methodology of Reference 2. These changes are discussed in Appendix A. The entropy can also be determined at each body location. If the bow shock is attached (sharp body), it is simply the entropy behind the bow shock. For blunt bodies, an iterative boundary layer mass balance technique is used to account for the gradient in entropy along the boundary layer edge created by the curved bow shock. This approach also represents a change from Reference 2 where the boundary layer edge entropy was assumed to be constant and equal to the entropy behind the normal shock at the nose tip. This constant entropy scenario indeed represents the true inviscid solution because the body will coincide with the stagnation streamline. However, the streamlines intersecting the edge of a boundary layer, which is increasing in thickness in the streamwise direction, originate from different points on the curved bow shock. Thus, the edge entropy varies from the stagnation value at the nose tip to some limiting downstream value based on the curvature of the outer bow shock. The details of this entropy computational technique are described in Appendix B.

A third property, the total enthalpy, h_0, is also known because the flow is adiabatic. The remaining fluid properties can then be determined.

4.3.1 Perfect Gas

As before, assume a constant specific heat, then proceed as follows:

$$c_p = \frac{\gamma}{\gamma - 1} \tag{4-69}$$

$$T = T_\infty \exp\left(\frac{S_b}{c_p} + \frac{R}{c_p} + \ln\left(\frac{p_b}{p_\infty}\right)\right) \tag{4-70}$$

$$\rho_b = \frac{p_b}{R\,T_b} \tag{4-71}$$

$$h_b = c_p\,T_b \tag{4-72}$$

$$a_b = \sqrt{\gamma\,R\,T_b} \tag{4-73}$$

$$v_b = \sqrt{2\,(h_0 - h_b)} \tag{4-74}$$

$$M_b = \frac{v_b}{a_b} \tag{4-75}$$

$$z_b = 1 \tag{4-76}$$

4.3.2 Real Gas

Computations proceed along the same lines as before with the curve fit relations being used.

$$\rho_b = \rho_b(p_b, S_b) \tag{4-77}$$

$$h_b = h_b(p_b, \rho_b) \tag{4-78}$$

$$a_b = a_b(p_b, S_b) \tag{4-79}$$

$$T_b = T_b(p_b, \rho_b) \tag{4-80}$$

$$e_b = h_b - \frac{p_b}{\rho_b} \tag{4-81}$$

$$v_b = \sqrt{2(h_0 - h_b)} \tag{4-82}$$

$$M_b = \frac{v_b}{a_b} \tag{4-83}$$

$$\gamma_b = \frac{h_b}{e_b} \tag{4-84}$$

$$z_b = \frac{p_b}{\rho_b R\, T_b} \tag{4-85}$$

$$Pr_b = Pr_b(T_b, \rho_b) \tag{4-86}$$

$$\mu_b = \mu_b(T_b, \rho_b) \tag{4-87}$$

4.3.3 Eckert Reference Enthalpy Flat Plate Heat Transfer

Given the appropriate fluid properties, the laminar and turbulent heat transfer rates are computed as[13]

$$\dot{q}_{w,l} = 0.332\,(Pr^*)^{-0.667}\,\frac{\rho^* v_b}{\sqrt{\dfrac{Re^*}{N_l}}} \tag{4-88}$$

and

$$\dot{q}_{w,t} = 0.185\,(Pr^*)^{-0.667}\,\frac{\rho^* v_b}{\left(\ln\left(\dfrac{Re^*}{N_t}\right)\right)^{2.584}} \tag{4-89}$$

The * conditions are evaluated at the reference enthalpy, h*.

$$h^* = 0.5\,(h_w + h_e) + 0.22\,(h_{aw} - h_e) \tag{4-90}$$

For a perfect gas, the reference temperature, T*, may be used.

$$T^* = 0.5\,(T_w + T_e) + 0.22\,(T_{aw} - T_e) \tag{4-91}$$

The e subscript once again denotes the conditions at the edge of the boundary layer and, in this case, corresponds to the b subscript. N_l and N_t are the laminar and turbulent Mangler transformation factors that are equal to 3.0 and 2.0, respectively. These factors provide an approximation to three-dimensional results even though the basic heat transfer relations were originally derived for a flat plate. The degree of turbulence is determined by first computing a local Reynolds number based on the boundary layer running length, s, and the local reference conditions.

$$Re^* = \frac{\rho^* v_b s}{\mu^*} \tag{4-92}$$

As before, if Re* is less than a user-specified lower limit, Re_L, the flow is assumed to be fully laminar. For Re* values greater than a specified upper limit, Re_U, the flow is assumed to be fully turbulent. For intermediate transitional values of Re* between Re_L and Re_U, the heat transfer is given by

$$\dot{q}_w = \dot{q}_{w,l} + \left(\frac{Re^* - Re_L}{Re_U - Re_L}\right)\dot{q}_{w,t} \tag{4-93}$$

The manner in which s is determined within the program is strictly correct only for zero angle of attack. It is computed along constant circumferential lines and is equivalent to the streamwise body coordinate, referenced to the stagnation point as origin. In actuality, s should be measured along surface streamlines. At zero angle of attack, the streamlines coincide with the body coordinate system, but as angle of attack increases, the windward-side streamlines tend to sweep around the body toward the leeward side. To include this effect in the aeroprediction heating analysis would have involved a considerable penalty in computational time, so the approximate approach was chosen. At high angles of attack, this approximation can adversely impact the results.

4.4 CONTROL SURFACES

The control surface heating is determined in a manner exactly analagous to that for the body. The boundary layer edge conditions are available from the appropriate aeroprediction subroutines and are incorporated directly into the Eckert Reference Enthalpy Flat Plate relations given by Equations 4-88 and 4-89. The Mangler transformation factors, N_l and N_t, are both set to one, since the flow is essentially two-dimensional along the surface of fins or wings and the original flat plate form of the equations is appropriate. The reference properties are computed as for the body surface, and the laminar/turbulent character of the flow is determined by comparing the local reference Reynolds number to the specified upper and lower limits. If the flow is transitional, Equation 4-93 is used. The boundary coordinate, s, is measured straight back at a constant radial distance from the leading edge. Because there can be some inboard or outboard component to the flow, this is only an approximation to the actual streamline distance. The error involved in this simplification is usually quite small, and any attempt to compensate for it would not be cost effective for present purposes.

5.0 RESULTS

Validation of the new heat transfer methodology was carried out in two steps. The first involved comparing results from aeroprediction with those from the MINIVER code for stagnation point and stagnation line flows and also for sharp cone and sharp wedge flows at zero angle of attack. MINIVER models these specialized configurations quite well, providing a good check for both heat transfer and inviscid boundary layer edge conditions. The latter comparisons served as further validation of the real-gas model previously incorporated into the aeroprediction code. In the second step of the validation process, computations were performed for spherically blunted cones at angle of attack. The resulting heat transfer rates were compared to values generated by more sophisticated numerical methods and to experimental measurements.

5.1 STAGNATION POINT

The free-stream conditions for these computations correspond to an altitude of 82,500 ft and Mach numbers of 7.73, 10, and 15. The nose radius was 0.01 in. and the surface temperature was set to 580 °R. Aeroprediction and MINIVER results for boundary layer edge pressure, density, temperature, and enthalpy, as well as recovery temperature and heat transfer rate, are shown in Tables 5-1 through 5-3. In general, results from the two codes differ by less than 2 percent for all variables. The only exceptions are the heat transfer rates at Mach 10 and 15 with differences of 2.4 and 3.6 percent, respectively. The primary reason for these discrepancies lies in the differing values of viscosity coefficient. MINIVER uses a modified Sutherland Law formulation to compute the coefficient of viscosity, while aeroprediction uses curve fits.[8,9] As the temperature increases, these two approaches give increasingly divergent values with the difference approaching 33 percent at Mach 15. The magnitude of this variation is not fully reflected in the heating rates because of their square root dependency on viscosity coefficient. There are also compensating differences in the Prandtl number. MINIVER uses a constant value of 0.72 while aeroprediction once again relies on the curve fits. Because the curve fits have a stated range of validity of up to 25,000 °R, they should offer the more accurate approach.

TABLE 5-1. NOSE STAGNATION POINT COMPARISONS, $M_\infty = 7.73$

Parameter	Aeroprediction	MINIVER
Pressure (lb/ft^2)	4080	4120
Density ($slug/ft^3$)	0.0005335	0.000540
Temperature (°R)	4501	4420
Enthalpy (ft^2/sec^2)	31121047	31038431
Recovery temperature (°R)	4501	4419
Heat transfer (BTU/ft^2-sec)	2170	2202

TABLE 5-2. NOSE STAGNATION COMPARISONS, $M_\infty = 10$

Parameter	Aeroprediction	MINIVER
Pressure (lb/ft^2)	6894	6900
Density ($slug/ft^3$)	0.0006453	0.000658
Temperature (°R)	5877	5924
Enthalpy (ft^2/sec^2)	50480874	50311629
Recovery temperature (°R)	5877	5924
Heat transfer (BTU/ft^2-sec)	4856	4974

TABLE 5-3. NOSE STAGNATION COMPARISONS, $M_\infty = 15$

Parameter	Aeroprediction	MINIVER
Pressure (lb/ft^2)	15640	15800
Density ($slug/ft^3$)	0.0008021	0.000816
Temperature (°R)	9501	9453
Enthalpy (ft^2/sec^2)	110577829	110214264
Recovery temperature (°R)	9501	9453
Heat transfer (BTU/ft^2-sec)	17254	17900

5.2 STAGNATION LINE

The second configuration considered was the stagnation line of a swept cylinder. As in the first case, free-stream conditions correspond to an altitude of 82,500 ft at Mach numbers of 7.73, 10, and 15. The cylinder radius was 0.01 in. with a surface temperature of 580 °R. The sweep angle was 53.13 deg. Representative results from these runs are shown in Tables 5-4 through 5-6. Agreement is good overall, with maximum differences of 2.5 percent or less except for heat transfer rates where discrepancies run somewhat higher for the reasons discussed previously. For the two higher Mach numbers, the laminar heating rates shown are higher than the corresponding turbulent rates. This situation can arise when the turbulent relations are applied at a Reynolds number that is below their range of validity. The results were still included in the tables because they provide further confirmation that the heating rate computations in aeroprediction are behaving as they should.

TABLE 5-4. SWEPT CYLINDER STAGNATION LINE COMPARISONS, $M_\infty = 7.73$

Parameter	Aeroprediction	MINIVER
Pressure (lb/ft^2)	1470	1480
Density ($slug/ft^3$)	0.0004266	0.00430
Temperature (°R)	1992	2004
Enthalpy (ft^2/sec^2)	12745350	12704919
Recovery temperature (°R)	4013	4025
Laminar heat transfer (BTU/ft^2-sec)	492	480
Turbulent heat transfer (BTU/ft^2-sec)	830	802

TABLE 5-5. SWEPT CYLINDER STAGNATION LINE COMPARISONS, $M_\infty = 10$

Parameter	Aeroprediction	MINIVER
Pressure (lb/ft^2)	2453	2490
Density ($slug/ft^3$)	0.0004742	0.000486
Temperature (°R)	2978	2978
Enthalpy (ft^2/sec^2)	19711317	19652980
Recovery temperature (°R)	5433	5516
Laminar heat transfer (BTU/ft^2-sec)	1870	1817
Turbulent heat transfer (BTU/ft^2-sec)	1125	1200

TABLE 5-6. SWEPT CYLINDER STAGNATION LINE COMPARISONS, $M_\infty = 15$

Parameter	Aeroprediction	MINIVER
Pressure (lb/ft^2)	5560	5570
Density ($slug/ft^3$)	0.0005942	0.000606
Temperature (°R)	5286	5286
Enthalpy (ft^2/sec^2)	41346321	41235184
Recovery temperature (°R)	8701	8482
Laminar heat transfer (BTU/ft^2-sec)	6727	6550
Turbulent heat transfer (BTU/ft^2-sec)	4526	4700

As a further check, two additional cylinder radii of 0.5 and 1.0 in. were run. Heat transfer rates for these cases are shown in Tables 5-7 and 5-8. Agreement between the two methods is consistent with the previous results.

TABLE 5-7. SWEPT CYLINDER STAGNATION LINE COMPARISONS, RADIUS = 0.5 IN.

M_∞	Code	Laminar Heat Transfer (BTU/ft^2-sec)	Turbulent Heat Transfer (BTU/ft^2-sec)
7.73	Aeroprediction MINIVER	117 113	207 220
10.0	Aeroprediction MINIVER	264 257	514 550
15.0	Aeroprediction MINIVER	951 926	2070 2200

TABLE 5-8. SWEPT CYLINDER STAGNATION LINE COMPARISONS, RADIUS = 1.0 IN.

M_∞	Code	Laminar Heat Transfer (BTU/ft^2-sec)	Turbulent Heat Transfer (BTU/ft^2-sec)
7.73	Aeroprediction MINIVER	83 80	180 190
10.0	Aeroprediction MINIVER	187 182	448 470
15.0	Aeroprediction MINIVER	673 650	1802 1900

5.3 SHARP CONE

For the sharp-cone computations, free-stream conditions were again taken to be Mach numbers of 7.73, 10, and 15 at an altitude of 82,500 ft. The cone half angle was 30 deg, and the heat transfer was computed at a point 1.75 in. from the nose tip stagnation point. Surface temperatures were 836 °R at Mach 7.73, 1200 °R at Mach 10, and 3658 °R at Mach 15. Representative results from aeroprediction and MINIVER for these conditions are shown in Tables 5-9 through 5-11. Agreement is good, with differences being well under 2 percent in most instances. The exception is the heat transfer rate at the highest Mach number where the turbulent values differ by 4.6 percent. The other heat transfer rates closely agree, a situation brought about by the lower temperatures involved in these computations relative to the stagnation conditions and a corresponding closer agreement in viscosity coefficients.

TABLE 5-9. 30-DEG SHARP-CONE COMPARISONS, $M_\infty = 7.73$

Parameter	Aeroprediction	MINIVER
Pressure (lb/ft^2)	1201	1210
Density ($slug/ft^3$)	0.0003888	0.000396
Temperature (°R)	1787	1782
Enthalpy (ft^2/sec^2)	11332032	11169005
Recovery temperature (°R)	3977	3986
Laminar heat transfer (BTU/ft^2-sec)	80.4	81.0
Turbulent heat transfer (BTU/ft^2-sec)	224	221

TABLE 5-10. 30-DEG SHARP-CONE COMPARISONS, $M_\infty = 10$

Parameter	Aeroprediction	MINIVER
Pressure (lb/ft^2)	1957	1980
Density ($slug/ft^3$)	0.0004384	0.000450
Temperature (°R)	2574	2561
Enthalpy (ft^2/sec^2)	16806866	16636016
Recovery temperature (°R)	5367	5460
Laminar heat transfer (BTU/ft^2-sec)	181	180
Turbulent heat transfer (BTU/ft^2-sec)	511	510

TABLE 5-11. 30-DEG SHARP-CONE COMPARISONS, $M_\infty = 15$

Parameter	Aeroprediction	MINIVER
Pressure (lb/ft^2)	4292	4350
Density ($slug/ft^3$)	0.0005449	0.000547
Temperature (°R)	4608	4606
Enthalpy (ft^2/sec^2)	32248110	33104186
Recovery temperature (°R)	8576	8387
Laminar heat transfer (BTU/ft^2-sec)	571	565
Turbulent heat transfer (BTU/ft^2-sec)	1652	1579

5.4 SHARP WEDGES

Once again, computations were performed for Mach numbers of 7.73, 10, and 15 at an altitude of 82,500 ft. The wedge half angle was 4 deg, and the wall temperature was a constant 580 °R. Heating rates were computed at a point 0.655 in. from the stagnation line. Results are shown in Tables 5-12 through 5-14. Agreement is once again good with boundary layer edge conditions differing by less than 3 percent and heat transfer rates by 4 percent or less.

TABLE 5-12. 4-DEG SHARP-WEDGE COMPARISONS, $M_\infty = 7.73$

Parameter	Aeroprediction	MINIVER
Pressure (lb/ft^2)	107	109
Density ($slug/ft^3$)	0.0001256	0.000127
Temperature (°R)	496	500
Enthalpy (ft^2/sec^2)	2982836	2992163
Recovery temperature (°R)	3763	3810
Laminar heat transfer (BTU/ft^2-sec)	26.6	25.6
Turbulent heat transfer (BTU/ft^2-sec)	53.4	51.0

TABLE 5-13. 4-DEG SHARP-WEDGE COMPARISONS, $M_\infty = 10$

Parameter	Aeroprediction	MINIVER
Pressure (lb/ft^2)	130	134
Density ($slug/ft^3$)	0.0001424	0.000146
Temperature (°R)	530	536
Enthalpy (ft^2/sec^2)	3184599	3211866
Recovery temperature (°R)	4858	4967
Laminar heat transfer (BTU/ft^2-sec)	53.2	51.5
Turbulent heat transfer (BTU/ft^2-sec)	104	100

TABLE 5-14. 4-DEG SHARP-WEDGE COMPARISONS, $M_\infty = 15$

Parameter	Aeroprediction	MINIVER
Pressure (lb/ft^2)	203	208
Density ($slug/ft^3$)	0.0001849	0.000189
Temperature (°R)	639	641
Enthalpy (ft^2/sec^2)	3707810	3842665
Recovery temperature (°R)	7303	7340
Laminar heat transfer (BTU/ft^2-sec)	162	158
Turbulent heat transfer (BTU/ft^2-sec)	301	300

5.5 SPHERICALLY BLUNTED CONES

The first configuration considered consisted of a 15-deg half-angle cone with a nose radius of 0.375 in. Free-stream pressure and temperature were 2.66 lb/ft^2 and 89.971 °R. The Mach number was 10.6 at an angle of attack of 20 deg. The wall temperature was 540 °R. Heat transfer rates along the windward symmetry plane are shown as a function of distance along the body in Figure 5-1. For comparison purposes, numerical results are shown from Reference 14 and corresponding experimental results from Reference 15. The methodology used in Reference 14 was much more involved than the approach employed in aeroprediction with the inclusion of complex streamline tracking methods and the axisymmetric analogue technique to model streamline spreading effects. Aeroprediction and MINIVER tend to underpredict the experimental data and the computational results of Reference 10 by 15 to 20 percent, a performance that is quite creditable considering the simplified solution approach. At the nose tip stagnation point, aeroprediction gives a heat transfer rate of 33.99 BTU/ft2-sec while Reference 14 predicts 35.94 BTU/ft2-sec, which again is good agreement.

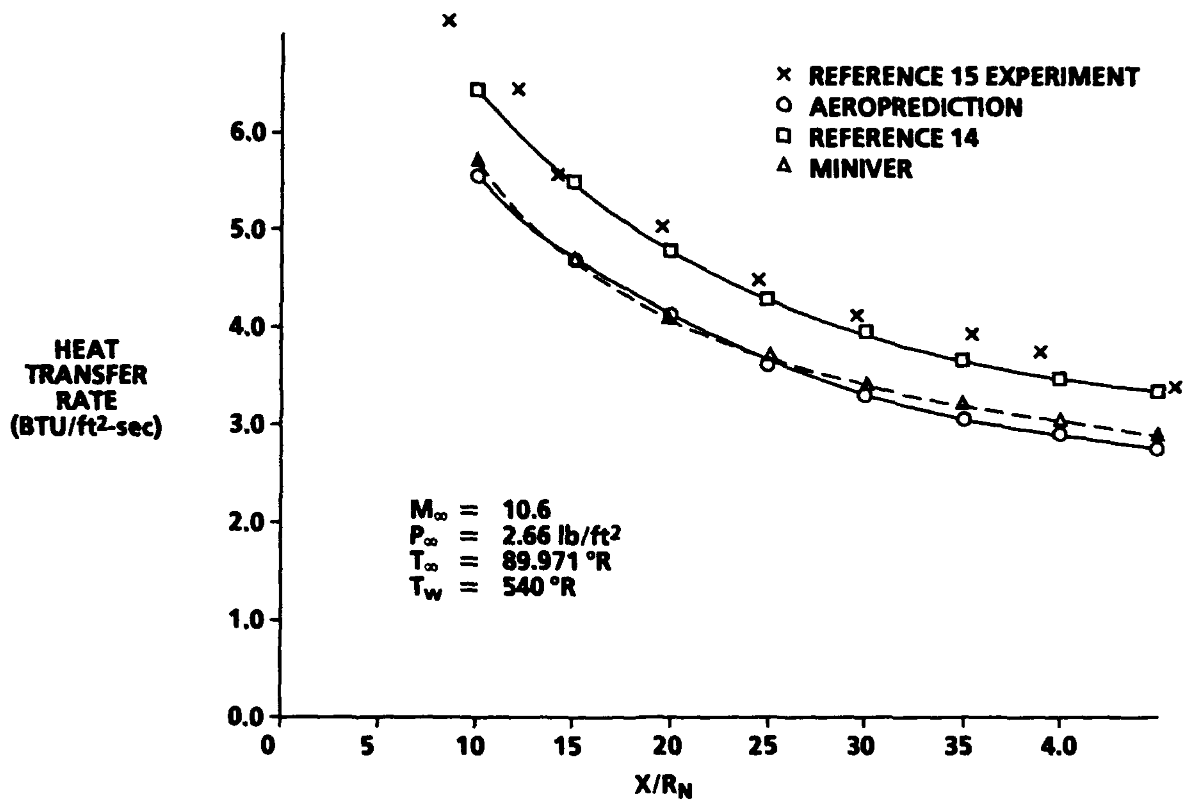

FIGURE 5-1. HEAT TRANSFER RATES FOR 0.375-IN. NOSE RADIUS, 15-DEG HALF-ANGLE CONE AT α = 20 DEG

The second configuration considered was a spherically blunted, 15-deg half-angle cone with a nose radius of 1.1 in. Free-stream pressure and temperature were 2.66 lb/ft^2 and 89.971 °R, respectively. The Mach number was 10.6 and angles of attack of 5 and 10 deg were run. The wall temperature was a constant 540 °R. Figures 5-2 and 5-3 show heating rate predictions on the windward symmetry plane as a function of position along the body for the 5- and 10-deg angle-of-attack cases, respectively. Also shown are results from AEROHEAT, an engineering type code that uses streamline tracking and axisymmetric analogue methodology, and from a second approximate code that uses more sophisticated streamline tracking, as well as a more exact boundary layer formulation.[16] MINIVER results are also plotted along with experimental data.[15] Aeroprediction does well beyond about 5 nose radii downstream but tends to overpredict heating rates near the nose tip. The region of overprediction is somewhat less at the higher angle of attack. This discrepancy is believed to be caused by the use of heating rate expressions that are based on flat plate relations and thus are incapable of modeling the effects of the rapidly changing boundary layer edge conditions in this region. The aeroprediction results are slightly better than those from MINIVER because of the inclusion of variable entropy effects. Figures 5-4 through 5-7 show the computed variation of heating rates in the circumferential direction around the body. The $\phi = 0$ location corresponds to the windward symmetry plane. Figures 5-4 and 5-5 illustrate results for a 5-deg angle of attack at points 4.86 and 10.13 nose radii downstream of the nose tip, respectively. At 4.86 nose radii, the aeroprediction results are uniformly high, a result that could be anticipated because of the tendency to overpredict heating rates in the nose region. At 10.13 nose radii, agreement with both numerical and experimental results is good, with the greater differences occurring on the leeward side of the body. Figures 5-6 and 5-7 show the 10-deg angle-of-attack results for the same streamwise locations. At the 4.86 nose radii station, except for the leeward plane, the aeroprediction results are actually more in agreement with the experiment than are the predictions of the more sophisticated numerical methodology of Reference 16. At 10.13 nose radii, the agreement is not as good but is still within 15 percent of both experimental data and other computational predictions. No results are shown from MINIVER for these circumferentially varying cases because it does not explicitly provide a capability to handle three-dimensional problems.

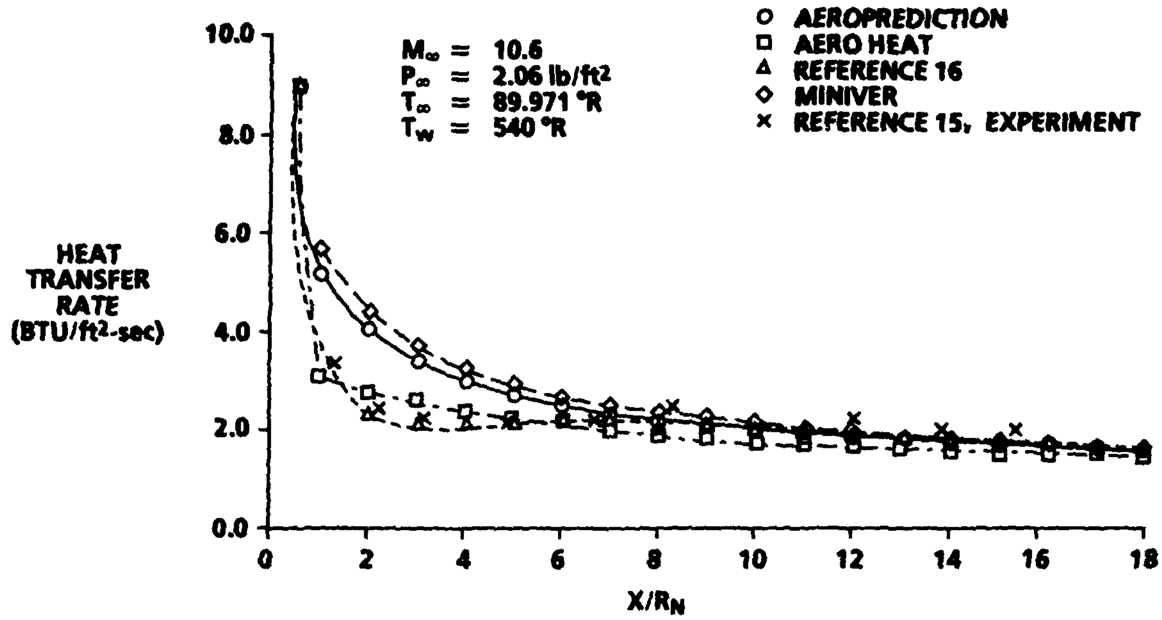

FIGURE 5-2. HEAT TRANSFER RATES FOR 1.1-IN. NOSE RADIUS, 15-DEG HALF-ANGLE CONE AT α = 5 DEG

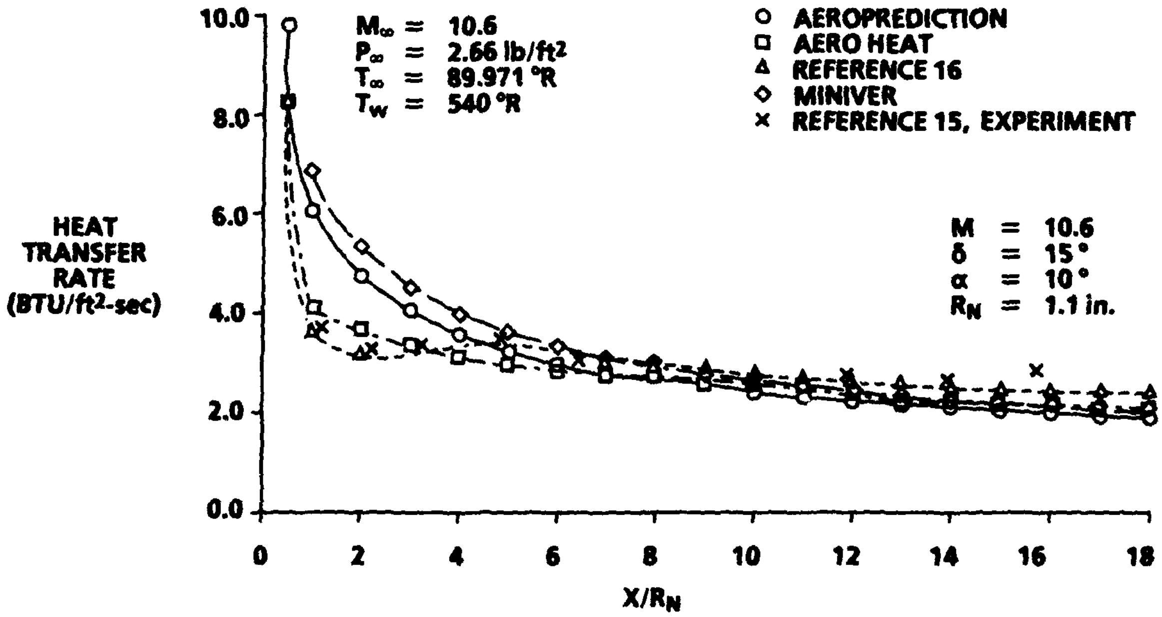

FIGURE 5-3. HEAT TRANSFER RATES FOR 1.1-IN. NOSE RADIUS, 15-DEG HALF-ANGLE CONE AT α = 10 DEG

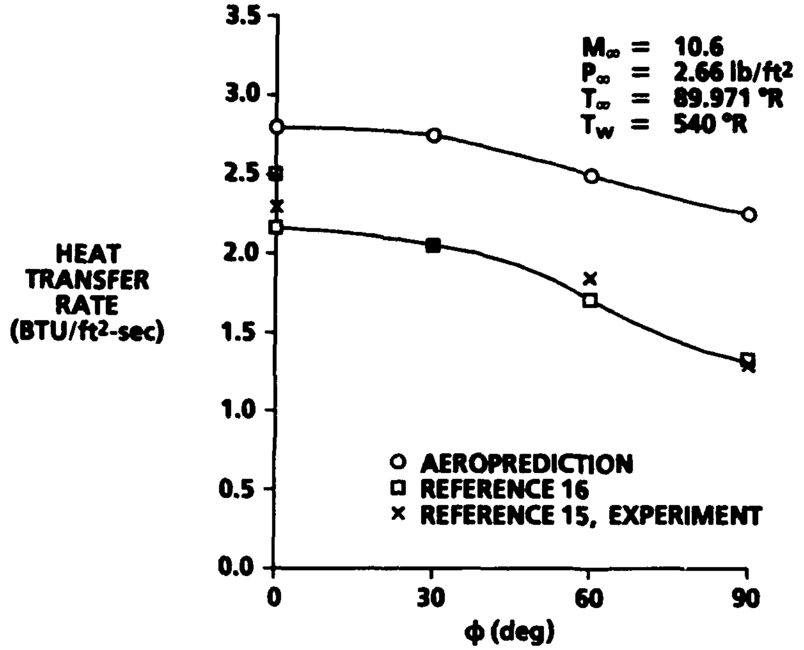

FIGURE 5-4. CIRCUMFERENTIAL VARIATION OF HEATING RATES ON 1.1-IN. NOSE RADIUS, 15-DEG HALF-ANGLE CONE AT α = 5 DEG, x/r_N = 4.86

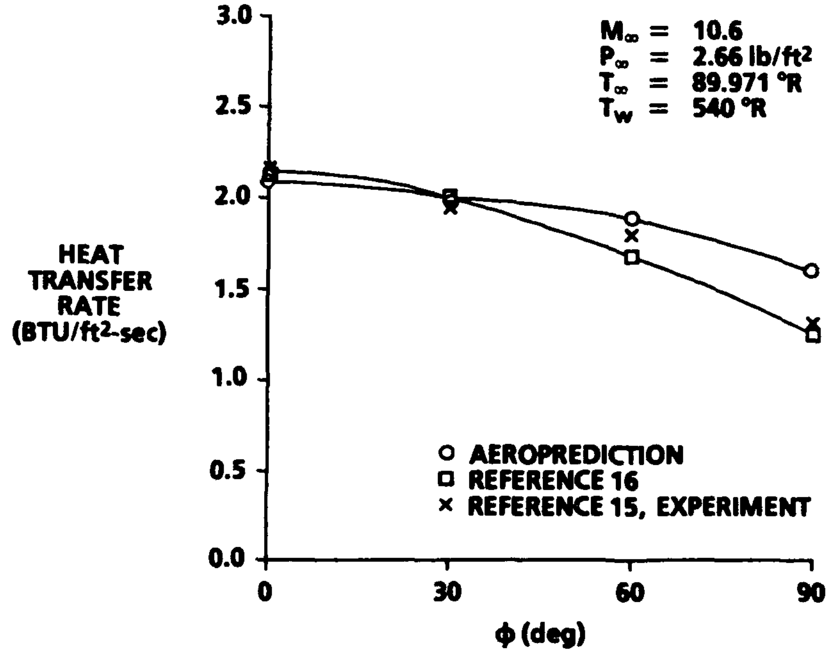

FIGURE 5-5. CIRCUMFERENTIAL VARIATION OF HEATING RATES ON 1.1-IN. NOSE RADIUS, 15-DEG HALF-ANGLE CONE AT α = 5 DEG, x/r_N = 10.13

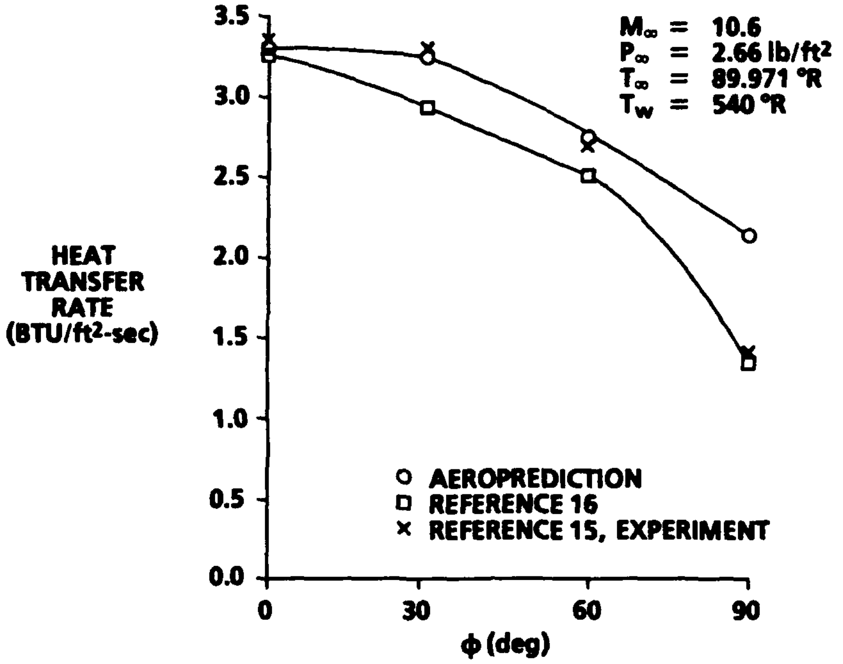

FIGURE 5-6. CIRCUMFERENTIAL VARIATION OF HEATING RATES ON 1.1-IN. NOSE RADIUS, 15-DEG HALF-ANGLE CONE AT α = 10 DEG, x/r_N = 4.86

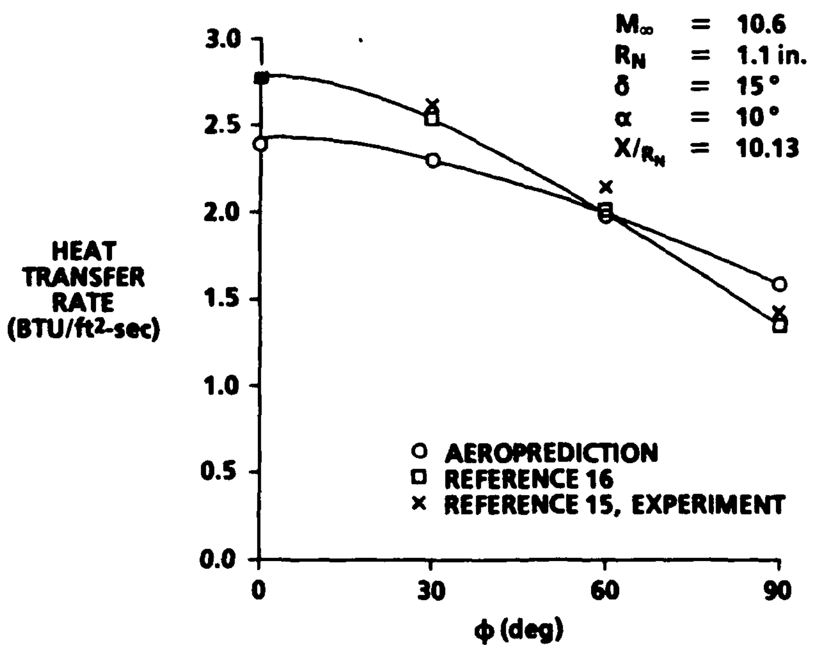

FIGURE 5-7. CIRCUMFERENTIAL VARIATION OF HEATING RATES ON 1.1-IN. NOSE RADIUS, 15-DEG HALF-ANGLE CONE AT α = 10 DEG, x/r_N = 10.13

6.0 SUMMARY

Methodology has been incorporated into the aeroprediction code to permit computation of heat transfer rates and recovery temperatures as part of the high Mach number solution. The aeroheating techniques implemented include a simplified Fay-Riddell model for the nose stagnation point, the Beckwith-Gallagher swept-cylinder method (modified to include real-gas effects) for control surface leading edges, and the Eckert reference enthalpy flat plate method for all other points on the body and control surfaces. A mass balance technique has been added to determine the appropriate entropy value to use as a boundary layer edge condition when solutions are computed for blunt bodies.

During the course of this work, refinements were made to the aeroprediction pressure methodology to achieve a better match point between the Improved Modified Newtonian Theory used on the forward portion of blunt bodies and the Second-Order Shock-Expansion Theory solution downstream of the nose region. Further modifications were made to remove discontinuities in the circumferential pressure distribution resulting in improvements in overall normal and axial force coefficients, especially for blunted cones.

Comparisons of heat transfer predictions from the updated code with those from more sophisticated engineering analysis methods and with experimental data show, in general, good agreement. There is a tendency to overpredict the heat transfer near the nose tip—a situation most likely arising from the inability of the methods used to account for the rapidly changing boundary layer edge conditions in this region.

Previously, most aeroheating analysis at NSWCDD has been done using either the MINIVER code or a combination ZEUS/boundary layer (ZEUSBL) approach. MINIVER has the advantage of being easy to implement and fast to run, producing time histories of surface temperatures at selected points with minimal effort. It suffers from an inability to model three-dimensional effects in an explicit manner or to account for a surface entropy layer. ZEUSBL can model three-dimensional effects well, but at the expense of much greater computational effort. It does, however, have the drawback of lacking a variable entropy model in its present form. The present method offers an approach to the aeroheating problem that, while not as sophisticated or rigorous as ZEUSBL, represents a definite improvement over MINIVER in analyzing bodies at angle of attack. It is also the superior method if surface entropy layer effects are significant. This added capability is gained at the expense of only a modest increase in computational effort.

7.0 REFERENCES

1. Anderson, J. D., *Hypersonic and High Temperature Gasdynamics*, McGraw-Hill Book Company, 1989.

2. Moore, F. G.; Armistead, M. A.; Rowles, S. H.; and DeJarnette, F. R., *Second-Order Shock-Expansion Theory Extended to Include Real Gas Effects*, NAVSWC TR 90-683, Feb 1992, NAVSWC, Dahlgren, VA.

3. Devan, L., *Aerodynamics of Tactical Weapons to Mach Number 8 and Angle of Attack 180°: Part I, Theory and Application*, NSWC TR 80-346, Oct 1980, NSWC, Dahlgren, VA.

4. Devan, L. and Mason, L., *Aerodynamics of Tactical Weapons to Mach Number 8 and Angle of Attack 180°: Part II, Computer Program and Users Guide*, NSWC TR 81-358, Sep 1981, NSWC, Dahlgren, VA.

5. Devan, L.; Mason, L.; and Moore, F. G., "Aerodynamics of Tactical Weapons to Mach Number 8 and Angle of Attack 180°," *American Institute of Aeronautics and Astronautics*, Paper No. 82-0250, 20th Aerospace Sciences Meeting, Orlando, FL, Jan 1982.

6. Moore, F. G., *Computational Aerodynamics at NAVSWC: Past, Present, and Future*, NAVSWC TR 90-569, Oct 1990, NAVSWC, Dahlgren, VA.

7. Wittliff, C. E. and Curtis, J. T., *Normal Shock Wave Parameters in Equilibrium Air*, Cornell Aero Laboratory Report CAL-III, Nov 1961.

8. Tannehill, J. C. and Mugge, P. H., *Improved Curve Fits for the Thermodynamic Properties of Equilibrium Air Suitable for Numerical Computations Using Time-Dependent or Shock Capturing Methods*, NASA CR-2470, 1974.

9. Srinivasan, S.; Tannehill, J.; and Weilmuenster, K., *Simplified Curve Fits for the Thermodynamic Properties of Equilibrium Air*, Report ISU-ERI-AMES 86401, Engineering Research Institute, Iowa State University, Ames, IA, Jun 1986.

10. Beckwith, I. E. and Gallagher, J. J., *Local Heat Transfer and Recovery Temperatures on a Yawed Cylinder at Mach Numbers of 4.15 and High Reynolds Numbers*, NASA Technical Report R-104, 1961.

11. Hender, D. R., *A Miniature Version of the JA70 Aerodynamic Heating Computer Program, H800(MINIVER)*, McDonnell-Douglas Astronautics Co., Report MDC G0462, Jun 1970.

12. Eckert, E. R. G., *Engineering Relations for Heat Transfer and Friction in High-Velocity Laminar and Turbulent Boundary Layer Flow over Surfaces with Constant Pressure and Temperature*, Transcript of the ASME, Vol. 78, No. 6, Aug 1956.

13. Eckert, E. R. G., *Survey of Boundary Layer Heat Transfer at High Velocities and High Temperatures*, WADC Technical Report 59-624, Apr 1960.

14. DeJarnette, F. R., *Calculation of Heat Transfer on Shuttle Type Configurations Including the Effects of Variable Entropy at Boundary Layer Edge*, NASA CR-112180, Oct 1972.

15. Cleary, J. W., *Effects of Angle of Attack and Bluntness on Laminar Heating Rate Distribution of a 15° Cone at a Mach Number of 10.6*, NASA TN D-5450, 1969.

16. Riley, C. J. and DeJarnette, F. R., "Engineering Aerodynamic Heating Method for Hypersonic Flow," *Journal of Spacecraft and Rockets*, Vol. 29, No. 3, May-Jun 1992.

8.0 SYMBOLS

a	Speed of sound (ft/sec)
C_A	Axial force coefficient
C_N	Normal force coefficient
c_p	Constant pressure specific heat (ft^2/sec^2-°R)
D	Diameter (ft)
e	Internal energy (ft^2/sec^2)
H	Temperature-based heat transfer coefficient (ft-lb/ft^2-sec-°R)
h	Enthalpy (ft^2/sec^2)
M	Mach number
N	Mangler transformation factor
Pr	Prandtl number
p	Pressure (lb/ft^2)
$\dot{q}$	Heat transfer (ft-lb/ft^2-sec or BTU/ft^2-sec)
R	Gas constant (ft^2/sec^2-°R)
R_c	Shock radius of curvature at vertex (ft)
Re	Reynolds number
r	Body or shock radius (ft)
r_c	Recovery factor
S	Entropy (ft-lb/slug-°R)

s	Boundary layer running length (ft)
T	Temperature (°R)
u	Velocity in streamwise direction (ft/sec)
v	Velocity (ft/sec)
x	Streamwise coordinate (ft)
z	Compressibility factor
α	Angle of attack (deg)
β	Limiting shock wave angle (deg)
γ	Specific heat ratio
δ	Boundary layer thickness (ft)
δ^*	Boundary layer displacement thickness (ft)
δ_c	Cone half angle (deg)
η	Enthalpy-based heat transfer coefficient (slug/ft^2-sec)
θ	Local body slope in streamwise direction (deg)
Λ	Control surface leading edge sweep (deg)
μ	Viscosity coefficient (slug/ft-sec)
ρ	Density (slug/ft^3)
ϕ	Circumferential angular coordinate (deg)
$\acute{\omega}$	Shock standoff distance (ft)

SUBSCRIPTS

aw	Adiabatic wall
b	Body
D	Diameter

DS	Downstream
e	Boundary layer edge
L	Lower transition limit
LE	Leading edge
l	Laminar
M	Match point
N	Nose tip
n	Normal direction
p	Parallel
S	Shock conditions
s	Based on boundary layer running length
t	Turbulent
U	Upper transition limit
w	Wall or surface
0	Stagnation conditions
2	Downstream of shock or expansion
∞	Free-stream conditions

SUPERSCRIPTS

$'$	Inviscid surface conditions behind parallel shock
*	Eckert reference conditions

APPENDIX A

MODIFICATIONS TO PRESSURE METHODOLOGY

For blunt bodies, the pressure prediction methodology of Reference A-1 involves a two-step procedure in which an improved modified Newtonian Technique (IMNT) is applied to the nose region and Second-Order Shock-Expansion Theory (SOSET) is used for the remainder of the body. Originally, the match point between the IMNT and SOSET regions was chosen to be the location at which the local body slope had decreased to 25.95 deg. It was found that using this fixed match point often resulted in pressure discontinuities of 10 to 15 percent. To eliminate this inconsistency, a parametric study was undertaken to determine the actual slope at which IMNT and SOSET produced equivalent pressures over a range of Mach numbers. The resulting Mach number/match point correlations were fit to a quadratic expression for match point as a function of Mach number.

$$\Theta_M = -0.028422619\,M^2 + 1.028273808\,M + 13.35357144 \tag{A-1}$$

Determining the match point in this manner decreases the pressure discontinuity to less than 2 percent in the Mach number range from 6 to 20, as shown in Table A-1. The error will be greater below Mach 6, but this pressure methodology would not normally be used for the lower Mach numbers. The results shown in Table A-1 represent zero angle-of-attack values. In aeroprediction, the zero incidence solution is computed first and then angle-of-attack effects are added by adjusting these pressures with an approximate analytical relation involving angle-of-attack, local body slope and body circumferential location. During this transformation process, the match point errors can sometimes increase slightly, but rarely do they exceed 2 percent, and in no case were they found to exceed 3 percent.

A second problem with pressure discontinuities was encountered that was associated with the manner in which the angle-of-attack corrections mentioned were applied. In Reference A-1, it was found that the use of a modified form of the pressure adjustment relations gave better results in the leeward planes for nonconical bodies. Unfortunately, it was found that using this modified formulation on the leeward side of blunted cones resulted in sharp pressure discontinuities in the circumferential direction. The code was modified to apply the pressure correction uniformly at all points for conical bodies and to slightly extend the region of modified corrections for the nonconical bodies from 30 to 60 deg away from the leeward body centerline. This procedure eliminated the discontinuities and, in terms of total coefficients as shown in Table A-2, gave much better results for cones and slightly better ones for ogives.

A-1 Moore, F. G.; Armistead, M. A.; Rowles, S. H.; and DeJarnette, F. R., *Second-Order Shock-Expansion Theory Extended to Include Real Gas Effects*, NAVSWC TR 90-683, Feb 1992, NAVSWC, Dahlgren, VA.

TABLE A-1. MATCH POINT VARIATION WITH MACH NUMBER

Mach Number	Body Slope at Match Point (deg)	Pressure Error (percent)
6	18.5	0.44
8	20.1	1.75
10	21.0	1.38
12	21.6	0.52
15	22.0	0.62
18	22.4	0.31
20	22.6	0.51

TABLE A-2. EFFECT OF PRESSURE MODIFICATIONS AT ANGLE OF ATTACK–M = 15, ANGLE OF ATTACK = 0 DEG

	20-Percent Blunt 15-Deg Cone		20-Percent Blunt Von Karman Ogive	
	C_N	C_A	C_N	C_A
Reference A-1	0.257	0.219	0.314	0.149
Present method	0.313	0.201	0.308	0.150
ZEUS	0.297	0.190	0.284	0.112

APPENDIX B

ENTROPY LAYER EFFECTS

To apply any boundary layer solution technique, it is first necessary to determine appropriate outer edge boundary conditions. One method of accomplishing this task is to first obtain an inviscid solution for the flow about the body of interest and then apply the surface conditions from this model as boundary layer edge conditions. For pointed bodies with attached shocks of uniform slope, this method provides physically consistent solutions. However, in the case of blunted objects, the situation becomes more involved. The true inviscid surface solution implies that the entropy along the body surface is a constant equal to the value behind the normal shock at the forward stagnation point. This situation results because of the constancy of entropy along streamlines and the fact that the body surface is coincident with the stagnation streamline. Two factors make the use of the constant normal shock entropy as the boundary layer edge condition inappropriate. First, the bow shock ahead of a blunt object is highly curved in the vicinity of the body. Thus, the streamlines lying near the body surface cross the shock at locations with different slopes resulting in different entropy values along each streamline. An *entropy layer* is created that flows back over the surface. The second complicating factor is the finite thickness of the boundary layer that increases in the streamwise direction. It is the value of entropy along the streamline that intersects the outer boundary layer that determines the appropriate edge properties to use in the viscous solution. Only if the boundary layer were of zero thickness would the edge entropy be the normal shock value. This situation is illustrated in Figure B-1.

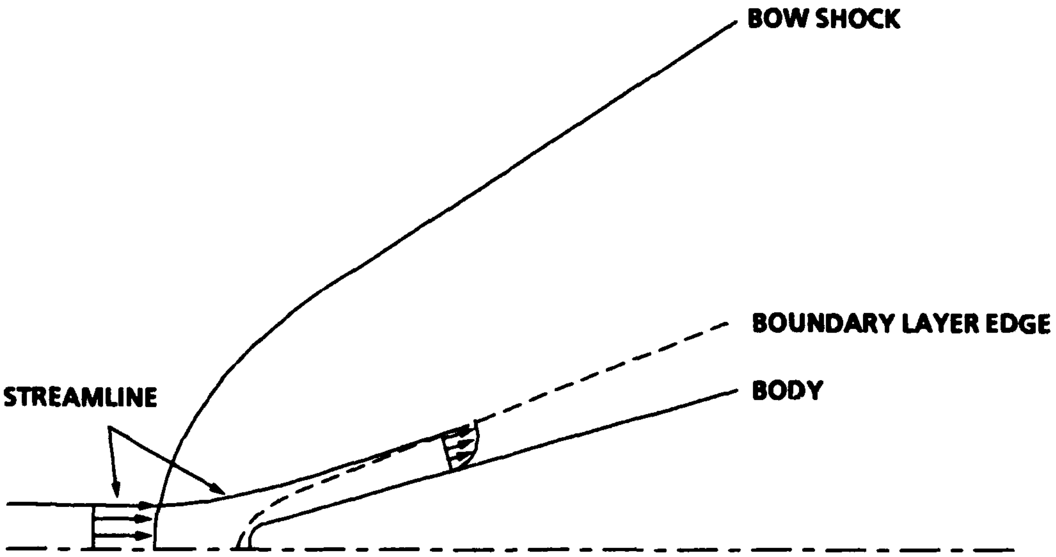

FIGURE B-1. DETERMINATION OF BOUNDARY LAYER EDGE ENTROPY ON BLUNT BODIES WITH HIGHLY CURVED BOW SHOCKS

To determine this local entropy value, a mass balance technique can be applied. The mass flux through a basically trapezoidal element bounded by the body surface and the boundary layer edge with a circumferential angular displacement $\Delta\phi$ is

$$m_b = \frac{1}{2}\rho_e V_e (r_b + \delta^* + \delta)(\delta - \delta^*)\Delta\phi \tag{B-1}$$

where

ρ_e = Density at boundary layer edge

V_e = Velocity at boundary layer edge

r_b = Local body radius

δ = Local boundary layer thickness

δ^* = Local boundary layer displacement thickness

At the shock, the mass flux through a triangular element $\Delta\phi$ in circumferential displacement and r_s in radius is

$$m_S = \frac{1}{2}\rho_\infty V_\infty r_S^2 \Delta\phi \tag{B-2}$$

where

ρ_∞ = Free-stream density

V_∞ = Free-stream density

If m_b and m_S are equated, it is possible to solve for r_S, which will be the radial location on the shock of the streamline that intersects the boundary layer at the local body point. This gives

$$r_S = \sqrt{\frac{\rho_e V_e}{\rho_\infty V_\infty}(2 r_b + \delta^* + \delta)(\delta - \delta^*)} \tag{B-3}$$

The determination of r_S is an iterative process, because the local boundary layer thickness is dependent on the local entropy. A value for entropy must be assumed, and in conjunction with the local pressure value that is known and is not affected by the boundary layer (to a first approximation), the other local thermodynamic properties can be determined. A boundary layer thickness is then computed. At the present time, this computation is done by basic incompressible relations with the use of Eckert's reference enthalpy properties to account for variations across the boundary layer. For laminar flow

$$\delta_1 = \frac{5.0\ s}{\sqrt{Re_s}} \tag{B-4}$$

$$\delta_1^* = \frac{1.729\ s}{\sqrt{Re_s}} \tag{B-5}$$

where s is the local boundary layer coordinate and Re_s is the Reynolds number based on s and the local reference enthalpy properties. For turbulent flow

$$\delta_t = \frac{0.37\ s}{(Re_s)^{0.2}} \tag{B-6}$$

$$\delta_t^* = \frac{0.046\ s}{(Re_s)^{0.2}} \tag{B-7}$$

For local Reynolds numbers below some lower value Re_L, the laminar values are used. For local Reynolds numbers above an upper limit Re_U, the turbulent value is used. For transitional cases with $Re_L < Re_s < Re_U$, the boundary layer thickness is given by

$$\delta = \delta_1 + \frac{Re_s - Re_L}{Re_U - Re_L}(\delta_t - \delta_1) \tag{B-8}$$

The Reynolds number adjusted value of δ^* is determined in a similar fashion. Knowing δ and δ^* for the assumed value of entropy, r_S can be determined. The shock slope at this location is determined by first assuming an analytical expression for the shock shape.[B-1]

$$x = R_N + \omega - R_c \cot^2\beta\,[(1 + \frac{R_s^2 \tan^2\beta}{R_c^2})^{1/2} - 1] \tag{B-9}$$

B-1 Anderson, J. D., *Hypersonic and High Temperature Gasdynamics*, McGraw-Hill Book Co., 1989.

R_N is the nose radius and ω is the shock standoff distance given by

$$\frac{\omega}{R_N} = 0.143 \exp\left[\frac{3.24}{M_\infty^2}\right] \tag{B-10}$$

R_c is the radius of curvature of the shock at its vertex (assuming a hyperbolic shock shape), which is given by

$$\frac{R_c}{R_N} = 1.143 \exp\left[\frac{0.54}{(M_\infty - 1)^{1.2}}\right] \tag{B-11}$$

β is the limiting shock wave angle downstream from the nose curvature region. By differentiating Equation B-9 to get dr_S/dx and evaluating it at r_S, the shock slope at this point can be found. Then, the change in entropy across the shock can easily be determined. If it matches the assumed value at the body point, then the original assumption was correct and the solution can proceed to the next body station. If not, a second value of entropy is assumed and the process is repeated. If this value also fails to match, then a variable secant iteration process can be started, which usually converges quite rapidly to the correct local entropy.

If the body under consideration is a blunted cone, the local entropy value will lie somewhere between that found behind a normal shock at the free-stream Mach number and that found behind the attached oblique shock associated with the solution for a sharp cone of the same half angle. Tables B-1 and B-2 show normal shock and sharp-cone entropy values for several cone angles. As shown, they can be substantially different with the difference increasing as the Mach number goes higher. Tables B-3, B-4, and B- 5 illustrate the effects of using the variable entropy approach at various streamwise stations on a blunted cone. Values are given for entropy, pressure, temperature, density, recovery temperature, and heat transfer rate for solutions using constant sharp-cone entropy, constant normal shock entropy, and variable entropy for the windward plane of a 15-deg cone at Mach 10.6 and angle of attack of 5 deg. Pressures, because of the boundary layer assumption, are not affected, but as can be seen, temperatures and densities can vary by almost a factor of three. A serendipitous result of the manner in which the primitive variables interact in the various cases is the relative small variation of heat transfer rates for the three entropy assumptions.

Figure B-2 gives an indication of how the entropy varies along the body surface as a function of distance downstream from the stagnation point using the present approach. As can be seen, at a distance of 50 nose radii downstream, the entropy values have largely stabilized to the sharp-cone value. Figure B-3 shows the differences in heat transfer created by using the variable entropy approach versus constant normal shock entropy for the case of the windward plane on a 15-deg cone at 10-deg angle of attack. The variable entropy solution gives slightly higher heat

transfer values, and the difference increases with increasing distance from the stagnation point, as would be expected. The discrepancies between the two methods are not great, typically being 10 to 15 percent at most.

TABLE B-1. NORMAL SHOCK AND CONE ENTROPIES, M = 8, ALTITUDE = 150,000 FT

Cone Half Angle (deg)	Normal Shock Entropy (ft^2/sec^2-°R)	Cone Entropy (ft^2/sec^2-°R)
5	60631	51914
10	60631	52206
15	60631	52924
20	60631	53917
25	60631	54963
30	60631	55962

TABLE B-2. NORMAL SHOCK AND CONE ENTROPIES, M = 15, ALTITUDE = 150,000 FT

Cone Half Angle (deg)	Normal Shock Entropy (ft^2/sec^2-°R)	Cone Entropy (ft^2/sec^2-°R)
5	69548	52139
10	69548	53706
15	69548	55766
20	69548	57632
25	69548	59374
30	69548	61391

TABLE B-3. ENTROPY EFFECTS ON 15-DEG CONE, X = 0.528 FT, M = 10.6, ALTITUDE = 150,000 FT, ANGLE OF ATTACK = 0 DEG, WINDWARD PLANE

Parameter	Cone Entropy	Stagnation Entropy	Variable Entropy
Entropy (ft^2/sec^2-°R)	45394	52308	51444
Pressure (lb/ft^2)	53.78	53.74	53.74
Temperature (°R)	376	1190	1036
Density ($slug/ft^3$)	0.000083229	0.000025946	0.000029760
Recovery temperature (°R)	1763	1854	1830
Heat transfer (BTU/ft^2-sec)	3.0	2.5	2.6

TABLE B-4. ENTROPY EFFECTS ON 15-DEG CONE, X = 1.025 FT, M = 10.6, ALTITUDE = 150,000 FT, ANGLE OF ATTACK = 0 DEG, WINDWARD PLANE

Parameter	Cone Entropy	Stagnation Entropy	Variable Entropy
Entropy (ft^2/sec^2-°R)	45394	52308	50605
Pressure (lb/ft^2)	53.78	53.74	53.74
Temperature (°R)	376	1190	906
Density ($slug/ft^3$)	0.000083229	0.000025946	0.000034120
Recovery temperature (°R)	1763	1854	1806
Heat transfer (BTU/ft^2-sec)	2.1	1.8	1.9

TABLE B-5. ENTROPY EFFECTS ON 15-DEG CONE, X = 2.033 FT, M = 10.6, ALTITUDE = 150,000 FT, ANGLE OF ATTACK = 0 DEG, WINDWARD PLANE

Parameter	Cone Entropy	Stagnation Entropy	Variable Entropy
Entropy (ft^2/sec^2-°R)	45394	52308	49135
Pressure (lb/ft^2)	53.78	53.74	53.74
Temperature (°R)	376	1190	429
Density ($slug/ft^3$)	0.000083229	0.000025946	0.000072911
Recovery temperature (°R)	1831	1854	1829
Heat transfer (BTU/ft^2-sec)	1.4	1.3	1.4

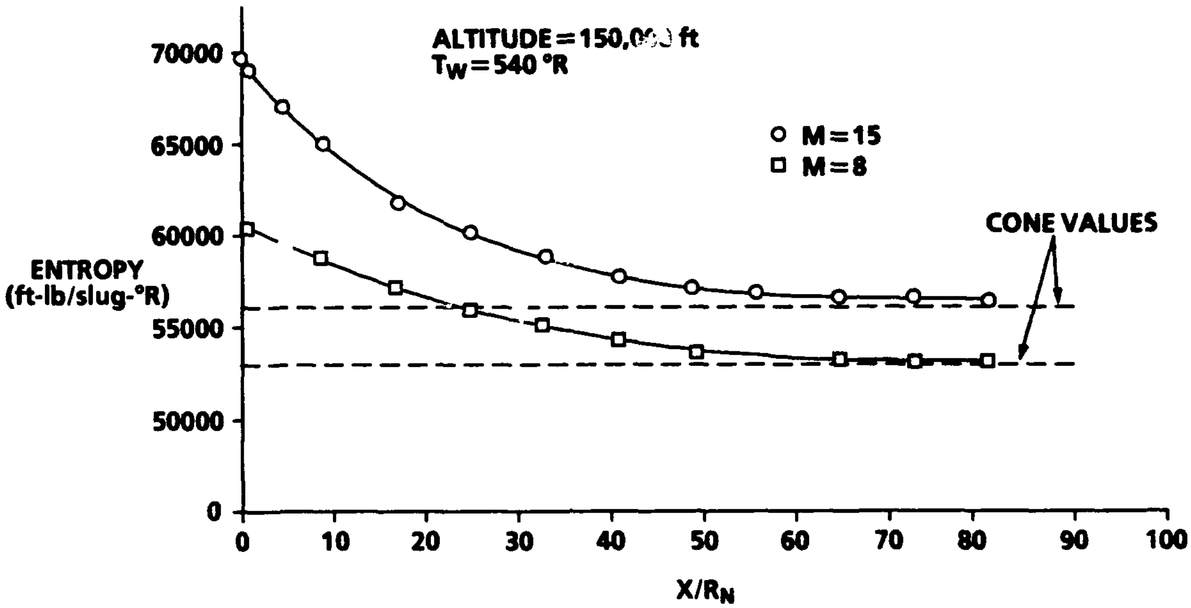

FIGURE B-2. VARIATION OF ENTROPY ALONG WINDWARD SYMMETRY PLANE OF 1.5-IN. NOSE RADIUS, 15-DEG HALF-ANGLE CONE

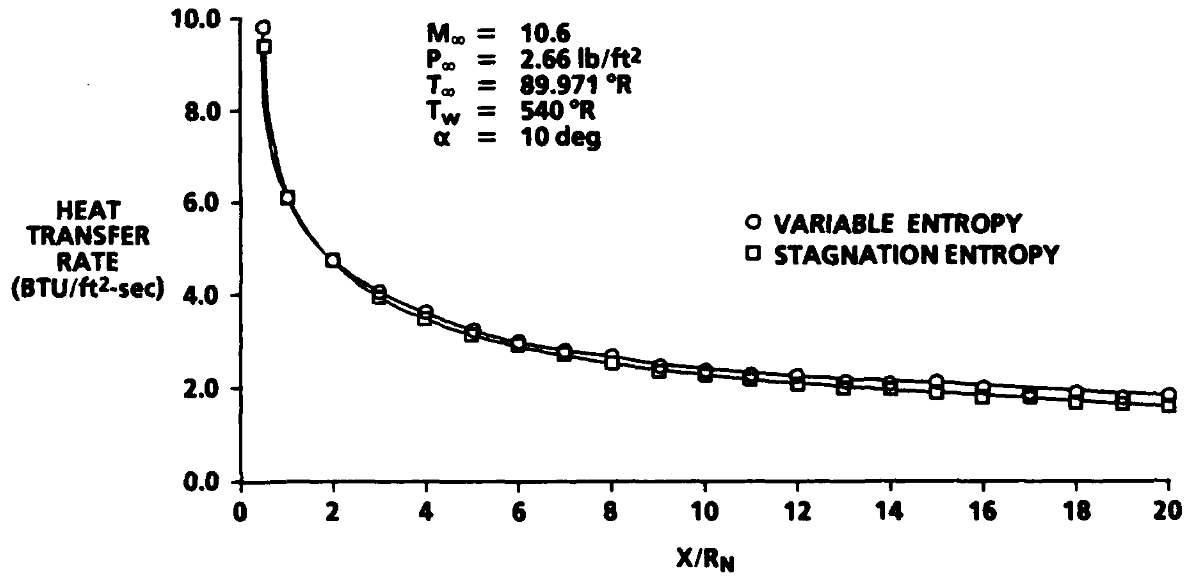

FIGURE B-3. EFFECT OF ENTROPY ON HEATING RATES ON WINDWARD SYMMETRY PLANE OF 1.1-IN. NOSE RADIUS, 15-DEG HALF-ANGLE CONE

DISTRIBUTION

	Copies
ATTN CODE 20 (SELWYN)	1
CODE 21 (ZIMET)	1
CODE 213 (SIEGEL)	1
CHIEF OF NAVAL RESEARCH OFFICE OF NAVAL RESEARCH 800 N QUINCY ST BCT #1 ARLINGTON VA 22217-5000	
ATTN CODE 1132F (LEKOUDIS)	1
CODE 12 (WOOD)	1
CODE 121 (HANSEN)	1
CODE 1215 (FEIN)	1
CHIEF OF NAVAL RESEARCH OFFICE OF NAVAL RESEARCH 800 N QUINCY ST BCT #1 ARLINGTON VA 22217-5000	
ATTN CODE C2891 (PORTER)	1
CODE C2892 (STRUTZ)	1
CODE C2892 (HALTER)	1
CODE C2894 (VAN DYKEN)	1
TECHNICAL LIBRARY	1
COMMANDER NAVAL AIR WARFARE CENTER WEAPONS DIVISION CHINA LAKE CA 93555-6001	
ATTN TECHNICAL LIBRARY	1
COMMANDER NAVAL SEA SYSTEMS COMMAND 2531 NATIONAL CITY BLDG 3 WASHINGTON DC 20362-5160	
ATTN AIR-53012D (JOHNSON) RM 904 JP2	1
TECHNICAL LIBRARY	1
COMMANDER NAVAL AIR SYSTEMS COMMAND WASHINGTON DC 20361-5300	
ATTN C KLEIN	1
TECHNICAL LIBRARY	1
COMMANDER NAVAL AIR WARFARE CENTER WEAPONS DIVISION POINT MUGU CA 93042-5000	

	Copies
ATTN T C TAI	1
M J MALIA	1
TECHNICAL LIBRARY	1
COMMANDER NAVAL SHIP RESEARCH AND DEVELOPMENT CENTER WASHINGTON DC 20034	
ATTN R M HOWARD	1
TECHNICAL LIBRARY	1
SUPERINTENDENT US NAVAL POSTGRADUATE SCHOOL MONTEREY CA 93943-5000	
ATTN S GREENHALGH	1
C REITZ	1
TECHNICAL LIBRARY	1
COMMANDING OFFICER NAVAL AIR WARFARE CENTER AIRCRAFT DIVISION WARMINSTER PA 18974-5000	
ATTN HEAD, WEAPONS DEPT	1
HEAD, SCIENCE DEPT	1
SUPERINTENDENT US NAVAL ACADEMY ANNAPOLIS MD 21402	
ATTN M KRUMINS	1
TECHNICAL LIBRARY	1
OFFICER IN CHARGE NAVAL INTELLIGENCE SUPPORT CENTER 4301 SUITLAND RD WASHINGTON DC 20390	
ATTN PAUL MURAD	2
DIAG DT 4T DEFENSE INTELLIGENCE AGENCY WASHINGTON DC 20546	
ATTN CODE 50255 (WAGGONER)	1
NAVAL WEAPONS SUPPORT CENTER CRANE IN 47522	

DISTRIBUTION (CONTINUED)

	Copies
ATTN CODE 5252P (KRAUSE)	1
TECHNICAL LIBRARY	1
COMMANDER	
INDIAN HEAD DIVISION	
NAVAL SURFACE WARFARE CENTER	
INDIAN HEAD MD 20640-5000	

ATTN TECHNICAL LIBRARY	1
DIRECTOR DEVELOPMENT CENTER	
MARINE CORPS DEVELOPMENT AND EDUCATION COMMAND	
QUANTICO VA 22134	

ATTN M TAUBER	1
TECHNICAL LIBRARY	1
AFATL (ADLRA) (DLGC)	
EGLIN AFB FL 32542-5000	

ATTN K COBB	1
E SEARS	1
L E LIJEWSKI	1
C COTTRELL	1
TECHNICAL LIBRARY	1
EGLIN AIR FORCE BASE FL 32542	

ATTN TECHNICAL LIBRARY	1
USAF ACADEMY	
COLORADO SPRINGS CO 80912	

ATTN G KURYLOWICH	1
D SHEREDA	1
J JENKINS	1
R SAMUELS	1
TECHNICAL LIBRARY	1
COMMANDING OFFICER	
AFSC	
WRIGHT PATTERSON AFB OH 45433	

ATTN TECHNICAL LIBRARY	1
ADVANCED RESEARCH PROJECTS AGENCY	
DEPARTMENT OF DEFENSE	
WASHINGTON DC 20305	

	Copies
ATTN J USSELTON	1
W B BAKER JR	1
TECHNICAL LIBRARY	1
ARNOLD ENGINEERING DEVELOPMENT CENTER USAF	
TULLAHOMA TN 37389	

ATTN TECHNICAL LIBRARY	1
NASA	
WASHINGTON DC 20546	

ATTN M TAUBER	1
TECHNICAL LIBRARY	1
NASA AMES RESEARCH CENTER	
MOFFETT CA 94035-1099	

ATTN C SCOTT	1
D CURRY	1
NASA JOHNSON SPACE CENTER	
HOUSTON TX 77058	

ATTN W C SAWYER	1
B HENDERSON	1
D MILLER	1
J ALLEN	1
F WILCOX	5
TECHNICAL LIBRARY	2
NASA LANGLEY RESEARCH CENTER	
HAMPTON VA 23365	

ATTN BILL WALKER	1
DAVE WASHINGTON	1
COMMANDING GENERAL	
AMSI RD SI AT	
REDSTONE ARSENAL AL 35898	

ATTN H HUDGINS	1
G FRIEDMAN	1
TECHNICAL LIBRARY	1
COMMANDING GENERAL	
ARRADCOM	
PICTINNY ARSENAL	
DOVER NJ 07801	
WASHINGTON DC 20013	

DISTRIBUTION (CONTINUED)

	Copies
ATTN C H MURPHY	1
R M McCOY	1
W STUREK	1
C NIETUBICZ	1
A MIKHAIL	1
P PLOSTINS	1
TECHNICAL LIBRARY	1
COMMANDING GENERAL	
BALLISTIC RESEARCH LABORATORY	
ABERDEEN PROVING GROUND	
MD 21005	
ATTN CODE TNC (BLACKLEDGE)	1
CDR AL KOREJO	1
DIRECTOR	
INTERCEPTOR TECHNOLOGY	
STRATEGIC DEFENSE INITIATIVE	
THE PENTAGON	
WASHINGTON DC 20350	
ATTN SFAE SD ASP	1
SFAE SD HED	1
DEPUTY COMMANDER	
US ARMY STRATEGIC DEFENSE COMMAND	
PO BOX 1500	
HUNTSVILLE AL 35807-3801	
ATTN PROF J A SCHETZ	1
VIRGINIA POLYTECHNIC AND STATE UNIVERSITY	
DEPT OF AEROSPACE ENGINEERING	
BLACKSBURG VA 24060	
ATTN F R DeJARNETTE	1
NORTH CAROLINA STATE UNIVERSITY	
DEPT OF MECHANICAL AND AEROSPACE ENGINEERING	
BOX 7921	
RALEIGH NC 27695	
ATTN J M WU	1
C BALASUBRAMAYAN	1
TECHNICAL LIBRARY	1
THE UNIVERSITY OF TENNESSEE SPACE INSTITUTE	
TULLAHOMA TN 37388	

	Copies
ATTN R NELSON	1
TECHNICAL LIBRARY	1
UNIVERSITY OF NOTRE DAME	
DEPT OF AEROSPACE AND MECHANICAL ENGINEERING	
BOX 537	
NOTRE DAME IN 46556	
ATTN E LUCERO	1
L TISSERAND	1
D FROSTBUTTER	1
TECHNICAL LIBRARY	1
APPLIED PHYSICS LABORATORY	
JOHNS HOPKINS UNIVERSITY	
JOHNS HOPKINS RD	
LAUREL MD 20707-6099	
ATTN D G MILLER	1
TECHNICAL LIBRARY	1
LAWRENCE LIVERMORE LAB	
EARTH SCIENCES DIVISION	
UNIVERSITY OF CALIFORNIA	
LIVERMORE CA 94550	
ATTN F PRILLMAN	1
W B BROOKS	1
R STANCIL	1
VOUGHT CORPORATION	
PO BOX 5907	
DALLAS TX 75222	
ATTN TECHNICAL LIBRARY	1
HUGHES AIRCRAFT CORPORATION	
CANOGA PARK CA 91304	
ATTN DR WALTER RUTLEDGE	1
R LaFARGE	1
R EISLER	1
WALTER RUTLEDGE (1635)	1
TECHNICAL LIBRARY	1
SANDIA NATIONAL LABORATORIES	
ALBUQUERQUE NM 87185-5800	
ATTN TECHNICAL LIBRARY	1
MARTIN MARIETTA AEROSPACE	
PO BOX 5837	
ORLANDO FL 32805	

DISTRIBUTION (CONTINUED)

	Copies
ATTN S SOPCZAK	1
TECHNICAL LIBRARY	1
HONEYWELL INC	
600 SECOND ST	
MINNEAPOLIS MN 55343	
ATTN B OMILIAN	1
CAL SPAN ADVANCED	
TECHNOLOGY CENTER	
PO BOX 400	
BUFFALO NY 14225	
ATTN TECHNICAL LIBRARY	1
ROCKWELL INTERNATIONAL	
MISSILE SYSTEMS DIVISION	
4300 E FIFTH AVE	
PO BOX 1259	
COLUMBUS OH 43216	
ATTN R CAVAGE	1
ADVANCED SYSTEMS DESIGN	
DEPT 113 407 (GB14)	
ROCKWELL	
NORTH AMERICAN AIRCRAFT	
OPERATIONS	
PO BOX 92098	
LOS ANGELES CA 90009	
ATTN G H RAPP	1
MOTOROLA INC	
MISSILE SYSTEMS OPERATIONS	
8201 E McDOWELL RD	
PO BOX 1417	
SCOTTSDALE AZ 85252	
ATTN R WYRICK	1
BOEING COMPUTER SERVICES INC	
PO BOX 24346	
SEATTLE WA 98124	

	Copies
ATTN J XERIKOS	1
N CAMPBELL	1
TECHNICAL LIBRARY	1
McDONNELL DOUGLAS ASTRONAUTICS	
CO (WEST)	
5301 BOLSA AVE	
HUNTINGTON BEACH CA 92647	
ATTN J WILLIAMS	1
S VUKELICH	1
J FIVEL	1
R GERBSCH (CODE 1111041)	1
TECHNICAL LIBRARY	1
McDONNELL DOUGLAS ASTRONAUTICS	
CO (EAST)	
BOX 516	
ST LOUIS MO 63166-0516	
ATTN M DILLENIUS	1
NIELSEN ENGINEERING AND	
RESEARCH INC	
510 CLYDE AVE	
MOUNTAIN VIEW CA 95043	
ATTN DR M FINK	1
UNITED TECHNOLOGIES	
NORDERN SYSTEMS	
MAIL STOP K041	
NORWALK CT 06856	
ATTN T LUNDY	1
D ANDREWS	1
TECHNICAL LIBRARY	1
LOCKHEED MISSILES AND SPACE	
CO INC	
PO BOX 1103	
HUNTSVILLE AL 35807	
ATTN L E ERICSSON	1
P REDING	1
TECHNICAL LIBRARY	1
LOCKHEED MISSILES AND SPACE	
CO INC	
PO BOX 504	
SUNNYVALE CA 94086	

DISTRIBUTION (CONTINUED)

	Copies
ATTN M WAREHAM RAYTHEON MISSILE SYSTEMS 50 APPLE HILL DR STOP T2SA9 TEWKSBURY MA 01876-0901	1
ATTN LLOYD PRATT AEROJET TACTICAL SYSTEMS CO PO BOX 13400 SACRAMENTO CA 95813	1
ATTN KURT HIVELY GENERAL DYNAMICS CONVAIR PO BOX 85357 SAN DIEGO CA 92138	1
ATTN SAM BLACK GOODYEAR AEROSPACE CORP 1210 MASSILLON RD AKRON OH 44315	1
ATTN W NORDGREN 721 GOULD INC OSD 18901 EUCLID AVE CLEVELAND OH 44117	1
ATTN DR Y C SHEN AEROJET ELECTRO SYSTEMS CO PO BOX 296 III AZUSA CA 91702	1
ATTN PETROS KYPRIOS TEXAS INSTRUMENTS INC PO BOX 405 MAIL STOP 3408 LOUISVILLE TX 75067	1
ATTN GERMAN MILITARY REP US OA GMR TRAFFIC AND TRANSPORTATION DIVISION 10 SERVICE RD DULLES INTERNATIONAL AP WASHINGTON DC 20041	1
ATTN DORIA GLADSTONE BATTELLE MEMORIAL INSTITUTE COLUMBUS DIVISION 505 KING AVE COLUMBUS OH 43201-2693	1
ATTN DR T P SHIVANANDA TRW ONE SPACE PARK REDONDO BEACH CA 90278	1
ATTN K C LEE ACCUREX CORP PO BOX 7040 520 CLYDE AVE MOUNTAIN VIEW CA 94039	1
ATTN A CHABOKI FMC CORPORATION 1300 S SECOND ST PO BOX 59043 MINNEAPOLIS MN 55459-0043	1
ATTN L FRENCH TRACOR AEROSPACE AUSTIN INC 6500 TRACO LANE AUSTIN TX 87825	1
ATTN ASO LO IS ISRAEL AIR FORCE LIAISON OFFICER 700 ROBBINS AVE PHILADELPHIA PA 19111	1
ATTN W J CLARK DYNA EAST CORPORATION 3132 MARKET ST PHILADELPHIA PA 19104	1
ATTN D SCHMITZ CHAMBERLAIN MANUFACTURING CORP RESEARCH AND DEVELOPMENT DIVISION PO BOX 2545 WATERLOO IA 50704-2545	1

DISTRIBUTION (CONTINUED)

	Copies
ATTN BRIAN WALKUP HERCULES AEROSPACE PRODUCT CO ALLEGHANY BALLISTIC LAB ROCKET CENTER WV 26726	1
ATTN ASSISTANT DEFENSE COOPERATION ATTACHE EMBASSY OF SPAIN WASHINGTON DC 20016	1
ATTN J FORKOIS KAMAN SCIENCES CORP 1500 GARDEN OF THE GODS RD PO BOX 7463 COLORADO SPRINGS CO 80933	1
ATTN M R D ANGELO MIT LINCOLN LABORATORY LEXINTON NA 02173-0073	1
ATTN M S MILLER DYNETICS INC PO DRAWER B HUNTSVILLE AL 35814-5050	1
ATTN H A McELROY GENERAL DEFENSE CORP PO BOX 127 RED LION PA 17356	1
ATTN R SEPLAK BRUNSWICK CORP DEFENSE DIVISION 3333 HARBOR BLVD COSTA MESA CA 92628-2009	1
ATTN J W McDONALD GENERAL RESEARCH CORP ADVANCED TECHNOLOGY INC 5383 HOLLISTER AVE PO BOX 6770 SANTA BARBARA CA 93160-6770	1
ATTN CAROL BUTLER OTI INTERNATIONAL 60 2ND ST SUITE 301 PO BOX 37 SHALIMAR FL 32579	1

	Copies
ATTN ARMAMENT SYSTEMS DEPT GENERAL ELECTRIC CO BURLINGTON VT 05401	1
ATTN JACK GRAMS TELEDYNE RYAN AERONAUTICAL 2701 HARBOR DR SAN DIEGO CA 92138	1
ATTN DR T LIN TRW ELECTRONICS AND DEFENSE SECTOR BLDG 527 RM 706 PO BOX 1310 SAN BERNADINO CA 92402	1
ATTN B S PRATS AIRTHERMOPHYSICS GENERAL ELECTRIC CO 3198 CHESTNUT ST PHILADELPHIA PA 19104	1
ATTN G VINCENT SPARTA INC 4301 CORPORATE DR HUNTSVILLE AL 35805	1
ATTN D P FORSMO	1
TECHNICAL LIBRARY RAYTHEON COMPANY MISSILE SYSTEMS DIVISION HARTWELL RD BEDFORD MA 01730	1
ATTN S PEARLSING	1
P GIRAGOSIAN RAYTHEON COMPANY SPENCER LABORATORY BOX SL7162 BURLINGTON MA 01803	1
ATTN NEILL S SMITH ARAP 1950 OLD GALLOWS RD SUITE 302 VIENNA VA 22180	1

DISTRIBUTION (CONTINUED)

	Copies
ATTN T R PEPITONE AEROSPACE TECHNOLOGY INC PO BOX 1809 DAHLGREN VA 22448	1
ATTN WILLIAM FACINELLI ALLIED SIGNAL PO BOX 22200 MS 1230 21E TEMPE AZ 85285	1
ATTN CDR R TEMPEST BRITISH NAVY STAFF WASHINGTON DC 20008	1
ATTN DENNIS BROWN NATIONAL AERONAUTICAL ESTAB NATIONAL RESEARCH COUNCIL MONTREAL RD OTTAWA ON CANADA K1A0R6	1
ATTN J EVANS DREV PO BOX 8800 COURCELETTE PQ CANADA GOA 1RO	1
ATTN H G KNOCHE	1
DR GREGORIOU MESSERSCHMIDT BOLKOW BLOHM GMBH UNTERNEHMENSBEREICH APPARATE MUNCHEN 80 POSTFACH 801149 BAYERN FED REP OF GERMANY (DFR)	1
ATTN DR DONALD SPRING AEROSPACE ENGINEERING DEPT AUBURN UNIVERSITY AL 36849-5338	1
ATTN BOB WHYTE ARROW TECH ASSOCIATES INC 1233 SHELBURNE RD D 8 SO BURLINGTON VT 05403	1
ATTN FU HO LING 1300 30TH ST APT E2 31 BOULDER CO 80303	1
ATTN PROF H F NELSON DEPT OF MECH AND AERO ENG UNIVERSITY OF MISSOUR ROLLA ROLLA MO 65401	1
DEFENSE TECHNICAL INFORMATION CENTER CAMERON STATION ALEXANDRIA VA 22314	12
ATTN GIFT AND EXCHANGE DIVISION LIBRARY OF CONGRESS WASHINGTON DC 20390	4
GIDEP OPERATIONS OFFICE CORONA CA 91720	1
DEFENSE PRINTING SERVICE WASHINGTON NAVY YARD WASHINGTON DC 20374	1

INTERNAL DISTRIBUTION

	Copies
C	1
D	1
D1	1
D2	1
D4	1
A	1
B	1
E	1
E231	3
E232	2
E281 (GARNER)	1
F	1
G	1
G02	1
G04	10
G05	1
G06	1
G07	1
G20	1
G205	1
G23	1
G23 (CHADWICK)	1
G23 (DEVAN)	1
G23 (HARDY)	1

DISTRIBUTION (CONTINUED)

	Copies
G23 (HYMER)	1
G23 (McINVILLE)	1
G23 (ROWLES)	1
G23 (WEISEL)	1
G30	1
G40	1
G23 (GRAFF)	1
G50	1
G60	1
G80	1
G90	1
GHO	1
GH3	1
K	1
K10	1
K20	1
K204	1
N.	1
N74 (GIDEP)	1
R	1
R44	1
R44 (PRIOLO)	1
R44 (HSIEH)	1
R44 (WARDLAW)	1

REPORT DOCUMENTATION PAGE

Form Approved
OMB No. 0704-0188

1. AGENCY USE ONLY *(Leave blank)*

2. REPORT DATE
February 1993

3. REPORT TYPE AND DATES COVERED

4. TITLE AND SUBTITLE
Incorporation of Boundary Layer Heating Predictive Methodology Into NSWCDD Aeroprediction Code

5. FUNDING NUMBERS

6. AUTHOR(S)
Roy M. McInville Frank G. Moore

7. PERFORMING ORGANIZATION NAME(S) AND ADDRESS(ES)
Naval Surface Warfare Center (G23)
Dahlgren Division
Dahlgren, VA 22448-5000

8. PERFORMING ORGANIZATION REPORT NUMBER
NSWCDD/TR-93/29

9. SPONSORING/MONITORING AGENCY NAME(S) AND

10. SPONSORING/MONITORING AGENCY REPORT NUMBER

11. SUPPLEMENTARY NOTES

12a. DISTRIBUTION/AVAILABILITY
Distribution authorized to U.S. Government agencies only; administrative/operational use (February 1993). Other requests for this document must be referred to NSWCDD (Code G23), Dahlgren, VA 22448-5000.

12b. DISTRIBUTION CODE

13. ABSTRACT *(Maximum 200 words)*

Methods have been incorporated into the Naval Surface Warfare Center, Dahlgren Division aeroprediction code to permit the computation of heat transfer rates and recovery temperatures as part of the high Mach number solution. A mass balance technique has been included to determine the correct boundary layer edge entropy to use along the surface of blunt bodies. Refinements were also made to the pressure prediction routines to remove discontinuities and improve overall results. Comparisons of results from the new methods with those from more advanced engineering codes, with other techniques of similar technical level of detail, and with experimental data sh ɔw good agreement. These new capabilities make possible the rapid computation of three-dimensional heat transfer information for a wide range of geometric configurations and flight conditions.

14. SUBJECT TERMS
aeroprediction code, high Mach number range, three-dimensional heat transfer rates, recovery temperatures, mass balance technique, boundary layer

15. NUMBER OF PAGES
69

16. PRICE CODE

17. SECURITY CLASSIFICATION OF REPORT	18. SECURITY CLASSIFICATION OF THIS PAGE	19. SECURITY CLASSIFICATION OF ABSTRACT	20. LIMITATION OF ABSTRACT
UNCLASSIFIED	UNCLASSIFIED	UNCLASSIFIED	SAR

GENERAL INSTRUCTIONS FOR COMPLETING SF 298

The Report Documentation Page (RDP) is used in announcing and cataloging reports. It is important that this information be consistent with the rest of the report, particularly the cover and its title page. Instructions for filling in each block of the form follow. It is important to ***stay within the lines*** to meet ***optical scanning requirements***.

Block 1. Agency Use Only *(Leave blank)*.

Block 2. Report Date. Full publication date including day, month, and year, if available (e.g. 1 Jan 88). Must cite at least the year.

Block 3. Type of Report and Dates Covered. State whether report is interim, final, etc. If applicable, enter inclusive report dates (e.g. 10 Jun 87 - 30 Jun 88).

Block 4. Title and Subtitle. A title is taken from the part of the report that provides the most meaningful and complete information. When a report is prepared in more than one volume, repeat the primary title, add volume number, and include subtitle for the specific volume. On classified documents enter the title classification in parentheses.

Block 5. Funding Numbers. To include contract and grant numbers; may include program element number(s), project number(s), task number(s), and work unit number(s). Use the following labels:

C	- Contract	**PR**	- Project
G	- Grant	**TA**	- Task
PE	- Program Element	**WU**	- Work Unit Accession No.

BLOCK 6. Author(s). Name(s) of person(s) responsible for writing the report, performing the research, or credited with the content of the report. If editor or compiler, this should follow the name(s).

Block 7. Performing Organization Name(s) and address(es). Self-explanatory.

Block 8. Performing Organization Report Number. Enter the unique alphanumeric report number(s) assigned by the organization performing the report.

Block 9. Sponsoring/Monitoring Agency Name(s) and Address(es). Self-explanatory.

Block 10. Sponsoring/Monitoring Agency Report Number. *(If Known)*

Block 11. Supplementary Notes. Enter information not included elsewhere such as: Prepared in cooperation with...; Trans. of...; To be published in.... When a report is revised, include a statement whether the new report supersedes or supplements the older report.

Block 12a. Distribution/Availability Statement. Denotes public availability or limitations. Cite any availability to the public. Enter additional limitations or special markings in all capitals (e.g. NOFORN, REL, ITAR).

DOD	- See DoDD 5230.24, "Distribution Statements on Technical Documents."
DOE	- See authorities.
NASA	- See Handbook NHB 2200.2
NTIS	- Leave blank

Block 12b. Distribution Code.

DOD	- Leave blank.
DOE	- Enter DOE distribution categories from the Standard Distribution for Unclassified Scientific and Technical Reports.
NASA	- Leave blank.
NTIS	- Leave blank.

Block 13. Abstract. Include a brief ***(Maximum 200 words)*** factual summary of the most significant information contained in the report.

Block 14. Subject Terms. Keywords or phrases identifying major subjects in the report.

Block 15. Number of Pages. Enter the total number of pages.

Block 16. Price Code. Enter appropriate price code ***(NTIS only)***

Block 17.-19. Security Classifications. Self-explanatory. Enter U.S. Security Classification in accordance with U.S. Security Regulations (i.e., UNCLASSIFIED). If form contains classified information, stamp classification on the top and bottom of this page.

Block 20. Limitation of Abstract. This block must be completed to assign a limitation to the abstract. Enter either UL (unlimited or SAR (same as report). An entry in this block is necessary if the abstract is to be limited. If blank, the abstract is assumed to be unlimited.